日本磁気学会
ISSN 2432-0250
Journal of the Magnetics Society of Japan
Electronic Journal URL: https://www.jstage.jst.go.jp/browse/msjmag

Vol.42 No.6　2018

Journal

JOURNAL OF THE MAGNETICS SOCIETY OF JAPAN

Vol.42 No.6 2018

日本磁気学会

ISSN 2432-0250

HP: http://www.magnetics.jp/ e-mail: msj@bj.wakwak.com

Electronic Journal: http://www.jstage.jst.go.jp/browse/msjmag

有限要素法解析ソフトウェア COMSOL Multiphysics®

COMSOL MULTIPHYSICS®

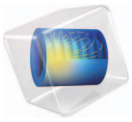

マルチフィジックスの進化論

無制限・強連成で実現象に即したシミュレーション事例のご紹介

永久磁石を利用した磁気軸受の解析例

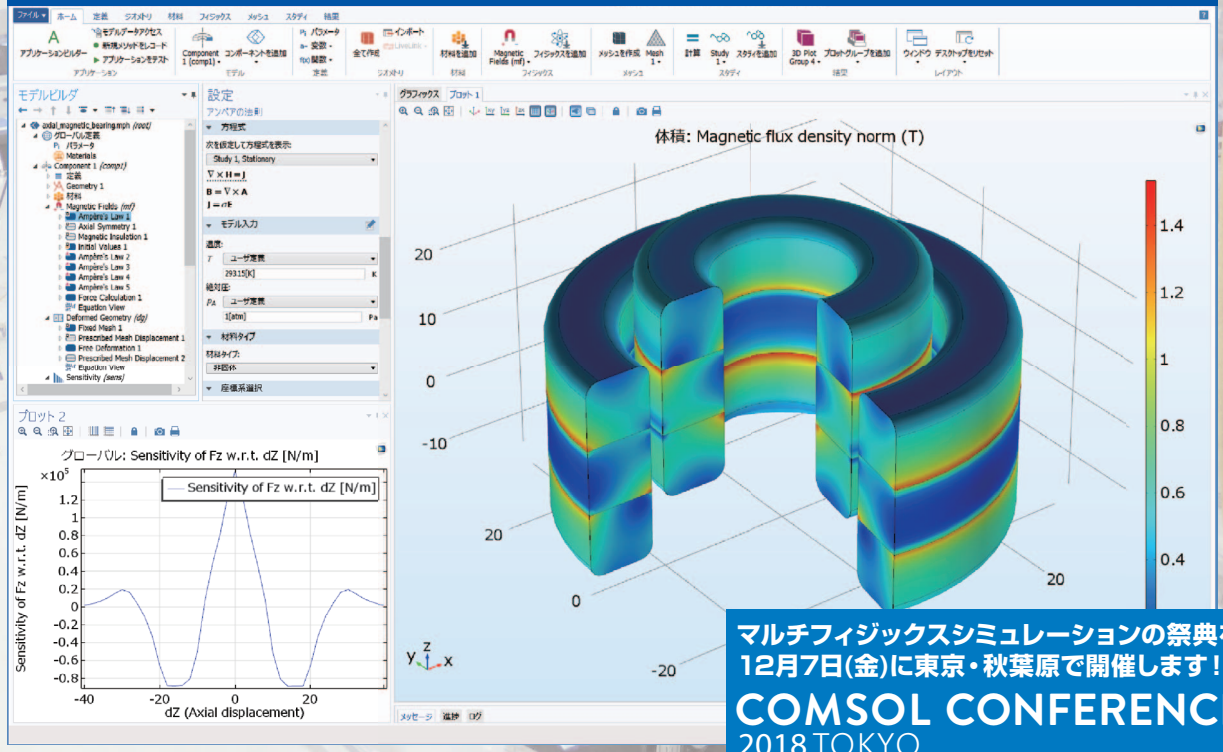

マルチフィジックスシミュレーションの祭典を12月7日(金)に東京・秋葉原で開催します！

COMSOL CONFERENCE 2018 TOKYO

Friday, December 7th, 2018 : Akihabara, Tokyo, JAPAN

http://www.kesco.co.jp/conference/

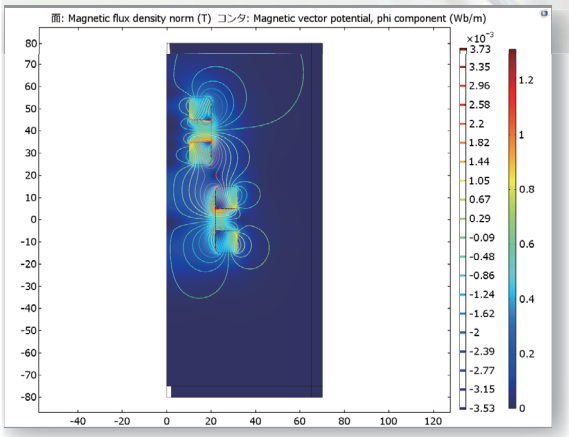

永久磁石を使用した磁気軸受

永久磁石を使用した軸受はターボ機械、ポンプ、モータ、発電機やフライホイール式エネルギー貯蔵システムなど、様々な分野で使用されています。非接触かつ潤滑不要で保守整備を大幅に省略できる点は、従来の機械式ベアリングと比べて重要なメリットです。この例では、軸方向の永久磁石軸受の磁気力と剛性などの設計パラメータを計算する方法を示しています。

※AC/DCモジュールはCOMSOL Multiphysicsと併用するアドオン製品です。

AC/DC モジュールの適用例

- AC/DC 電流分布、電場分布
- バイオヒーティング
- コイルとソレノイド
- SPICE 回路とフィールドシミュレーション
- 接触抵抗
- 電磁両立性 (EMC) および電磁妨害 (EMI)
- 電磁力およびトルク
- 電磁力シールド
- 電気機械の変形
- ホール効果を利用したセンサ
- インシュレータ、コンデンサ、誘電体
- モータ、ジェネレータ、および他の電気機械
- 非線形材料
- 寄生容量とインダクタンス
- 永久磁石と電磁石
- 多孔質材料
- 抵抗および誘導加熱
- センサ
- 超伝導体
- 変圧器とインダクタ

COMSOL Multiphysics® なら、今まで不可能だった 3 種以上のマルチフィジックス解析を強連成で実現できます。30 日間全機能無料トライアル、無料の導入セミナー、1000種を超える世界の様々な事例をご提供いたします。詳しくは、下記の弊社営業部までお問い合せください。

COMSOL

http://www.comsol.jp

COMSOLご紹介無料セミナー開催！

東京(神田)会場：2019年1月23日 13:30-16:30

皆様の拠点へお伺いして開催可能！お問い合わせください

詳細→ http://www.kesco.co.jp/comsol_intro.html

KESCO KEISOKU ENGINEERING SYSTEM

計測エンジニアリングシステム株式会社

http://www.kesco.co.jp/comsol/

Tel : 03-5282-7040 ・ Fax : 03-5282-0808

世界初！
高温超電導型VSM

新製品

世界初*、高温超電導マグネットをVSMに採用することで
測定速度 当社従来機1/20を実現。
0.5mm cube磁石のBr, HcJ高精度測定が可能と
なりました。
*2014年7月 東英工業調べ

測定結果例

高温超電導VSMによるNdFeB(sint.) 0.5mm cube BHカーブ

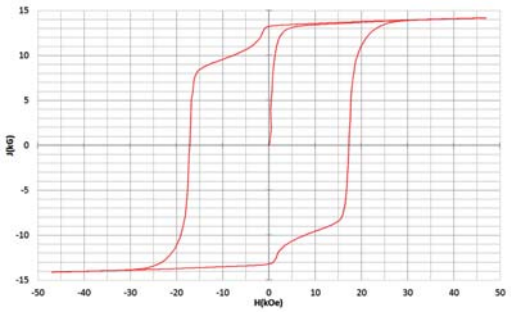

磁化測定レンジ：0.2emu
Br = 13.2kG　　HcJ = 17.2kOe

高温超電導VSMによるNdFeB(sint.) 1mm cube BHカーブ

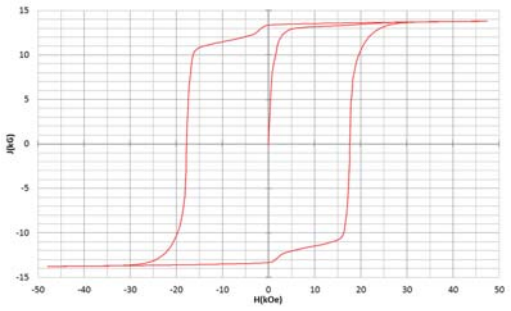

磁化測定レンジ：2emu
Br = 13.3kG　　HcJ = 17.7kOe

高温超電導VSMによるNdFeB(sint.) 4mm cube BHカーブ

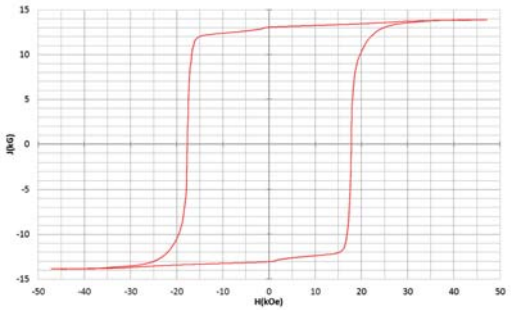

磁化測定レンジ：100emu
Br = 13.1kG　　HcJ = 17.8kOe

高速測定を実現

高温超電導マグネット採用により、高速測定を実現しました。Hmax= 5Tesla, Full Loop 測定が2分で可能です。
（当社従来機：Full Loop測定　40分）

小試料のBr,HcJ高精度測定

0.5mm cube 磁石のBr,HcJ高精度測定ができ、表面改質領域を切り出しBr,HcJの強度分布等、微小変化量の比較測定が可能です。
また、試料の加工劣化の比較測定が可能です。

試料温度可変測定

−50℃～+200℃温度可変UNIT（オプション）

磁界発生部の小型化

マグネットシステム部寸法：0.8m×0.3m×0.3m

TOEI 東英工業株式会社
http://www.toeikogyo.co.jp
〒194-0035 東京都町田市忠生1-8-13
TEL：042-791-1211　FAX：042-792-0490
E-mail : sales@toeikogyo.co.jp

Journal of the Magnetics Society of Japan
Vol. 42, No. 6

Electronic Journal URL: https://www.jstage.jst.go.jp/browse/msjmag

CONTENTS

J. Magn. Soc. Jpn., **42**, 119-126 (2018)

<Review>

Magnetoelectric control of antiferromagnetic domain of Cr_2O_3 thin film toward spintronic application

Y. Shiratsuchi, T. V. A. Nguyen and R. Nakatani

Graduate School of Engineering, Osaka University, *2-1 Yamadaoka, Suita, Osaka 565-0871, Japan*

Cr_2O_3 is a magnetoelectric antiferromagnet, and its antiferromagnetic domain state is controllable by the simultaneous application of magnetic and electric fields. In the 2000s, that is, more than 50 years since the discovery of the magnetoelectirc effect in Cr_2O_3, efforts were initiated apply this effect to engineering applications. In this article, we review the recent progress of the magnetoelectric control of the antiferromagnetic domain state and the related phenomena of Cr_2O_3, in particular, in an all-thin film system, an essential step to the application.

Key words: magnetoelectric effect, antiferromagnetic domain, Cr_2O_3, thin film

1. Introduction

The interplay between magnetism and electricity has been known as the magnetoelectric (ME) effect, which is referred as the magnetization (M) induction caused by an electric field (E) and the electric polarization (P) induction caused by a magnetic field (H). The ME effect was predicted in the 19th century by Curie[1]. In 1920s, Perrier and Staring investigated this effect using Fe and Ni and proposed the existence ME effect[2,3]. Later on, however, they corrected their experiment was wrong[4]. Meantime, Piccard suggested the impossibility of the effect on symmetry grounds[5]. After these research, Debye who first used the term of "magneto-electric" suggested that the ME effect was impossible[6] and Van Vleck described in his book the reason why the ME effect was impossible[7]. After 50 years later from the Curie's proposal, Landau and Lifshitz dealt with this problem and showed that the ME effect should exit in magnetic crystal.[8] Based on the prediction by Landau and Lifshitz, Dzyaloshinskii predicted that Cr_2O_3 was an actual candidate causing this effect[9]. Soon after the prediction, the H-induced polarization P[10] and E-induced magnetization M[11] were experimentally confirmed independently. After the discovery of the ME effect in Cr_2O_3, the research on this effect progressed to the field of "multiferroics"[12]. More details about the history of the ME effect can be found in textbook[13] and the progress of the ME effect after the early development can be found in previous review[14].

As Cr_2O_3 exhibits a linear ME effect, the removing field disperses the ferroic feature. This could partly be the reason why efforts to apply the ME effect of Cr_2O_3 to engineering applications were not very active until the pioneering work by Borisov *et al.*[15]. Their idea is based on the fact that to complement the limitation of the linear ME effect, the ferromagnetic (FM) layer coupled with Cr_2O_3 was used as a marker of the ME-controlled antiferromagnetic (AFM) order parameter. The interfacial exchange coupling between FM and AFM spins results in the exchange bias[16-18] and the exchange bias polarity is, in principle, determined by the interfacial AFM spin direction. Based on this fundamental, they demonstrated that the exchange bias polarity could be reversed by the so-called ME-field cooling (MEFC) method. In this scenario, to switch the exchange bias polarity, temperature increase was necessary, that is, the system was required to be initialized by heating the sample above the Néel temperature. In 2010, He *et al.*[19] developed this technique in the isothermal mode. However, these two studies adopted the bulk Cr_2O_3 substrate, and thus the realization of the ME effect in the *all-thin-film* system, which is essential to the device application, was challenging.

Before the achievement of the ME effect through the Cr_2O_3 thin film, some studies theoretically analyzed surface magnetization[20] (or boundary magnetization[21]). It was supposed that the ME switching of the exchange bias polarity was due to the electrically controllable boundary magnetization that coupled with the AFM order parameter[19,21]. In 2014, we presented the experimental evidence of the boundary magnetization on $Cr_2O_3(0001)$[22] including the roughness-insensitive magnetization, absence of the training effect of exchange bias, and ME switching. Nowadays, owing to the achievement of both the MEFC[22-24] and isothermal switching[25-28] in an *all-thin-film* system, we can access the details of the ME switching such as the energy condition of the switching[27] and switching dynamics[28]. In this paper, we review the recent progress of the ME control of the AFM domain state of Cr_2O_3, mainly based on our own results as the subject of the magnetic society of Japan (MSJ) outstanding research award 2017.

2. Magnetoelectric control of AFM Cr_2O_3 domain state

In Cr_2O_3, the Cr^{3+} spin lies along the c axis, and the spin direction is contradictory at the neighbored c plane (Fig. 1). According to this spin alignment, $Cr_2O_3(0001)$ thin film is suitable for inducing the perpendicularly-directed exchange bias that meets the recent requirement of the spintronic devices. In reality, a high perpendicular exchange magnetic anisotropy J_K above 0.4 mJ/m^2 was reported, which can be altered using

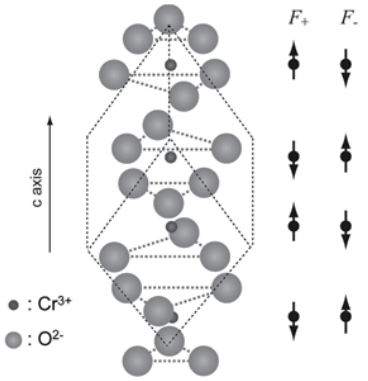

Fig. 1 Crystal structure and spin alignment of Cr_2O_3

different underlayers by alternating the crystal parameters (the lattice parameters and specific ion positions of Cr^{3+} and O^{2-} ion)[29]. Furthermore, in contrast to the fact that the coercivity enhancement is sometimes accompanied with the exchange bias, the coercivity enhancement of the FM/Cr_2O_3 stacked film can be suppressed using a suitable spacer layer at the FM/Cr_2O_3 interface[30]. Details about the exchange bias can be found in some previous reviews[16-18] and, in particular that about the perpendicular exchange bias using a Cr_2O_3(0001) film can be found in our previous review[31], respectively.

According to the above-mentioned spin alignment, two magnetic domains with the opposite Cr^{3+} spins are energetically degenerated (Fig. 1). The free energy of the two domains under both electric field E and magnetic field H is expressed by[32]

$$F_{\pm} = F_0 + \sigma_i H_i + \rho_i E_i + 1/2\ \chi_{ij} H_i H_j + 1/2\ \chi_{ij}' E_i E_j \pm \alpha_{ij} E_j H_j + \ldots \quad (1)$$

where the first term (F_0) is a constant; σ_i and ρ_i are pyromagnetic and pyroelectric coefficients, respectively; χ_{ij} and χ'_{ij} are magnetic and dielectric susceptibility, respectively; and α_{ji} is the ME coefficient. The second and third terms represent the pyromagnetism and pyroelectric polarizations, respectively, which can be eliminated for Cr_2O_3 because of its crystallographic symmetry.[32] The fourth and fifth terms represent the magnetization and electric polarization, respectively, and the sixth term represents the ME effect. The sign of the sixth term depends on the AFM order parameter of the two AFM domains. F_+ and F_- denote the free energies of the two domains. Equation (1) indicates that the energy difference of

$$\Delta F = 2\alpha_{ij} E_i H_j \quad (2)$$

was generated for the two domains by simultaneously applying the electric E and magnetic H fields, i.e., the degeneration was broken. Consequently, two AFM domains become selectable. Since the exchange bias of the film is determined by the AFM domain state[33,34] and is controllable by the ME effect. Till date, two types of ME-induced switching protocols have been proposed: MEFC and isothermal processes. In the following section, we describe the results for each process.

2.1 MEFC process

MEFC is a cooling method in which the magnetic and electric fields are simultaneously applied during the cooling from above the Néel temperature of Cr_2O_3 (~307 K)[10,35]. In this process, the AFM domain state is determined by the energy competition between the interfacial exchange coupling and ME effect on the onset of the AFM ordering. When electric field E is below the threshold value, the interfacial exchange coupling dominates the AFM domain state, and the exchange bias polarity is then determined by the magnetic field (more precisely, the FM spin direction) during the cooling. This situation is similar to the conventional field-cooling (FC) process. In contrast, when electric field E exceeds the threshold value, the energy gain due to the ME effect, proportional to the product of E and H (EH product, see eq. (2)) overcomes the interfacial exchange coupling energy. As a result, the exchange bias polarity is the opposite of that obtained in the previous case.

As a model system to assess the above-mentioned argument, we adopted the Pt/Co(/Pt)/Cr_2O_3/Pt thin film exhibiting a perpendicular exchange bias. The details of the film fabrication and the structural details can be found in refs. 29 and 30. To detect the exchange bias polarity, we measured the magnetization curve based on the anomalous Hall effect (AHE) measurements using

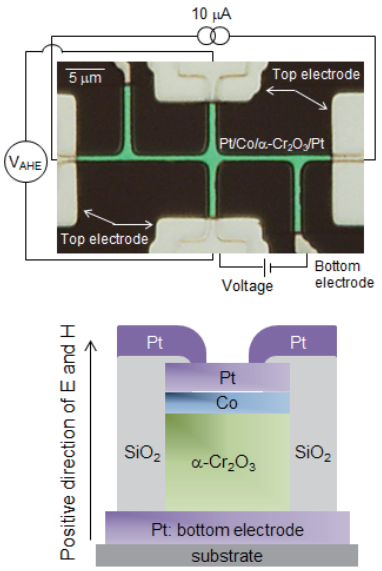

Fig. 2 Optical microscope image of the micro-fabricated Hall device with the measurement setup. The bottom image represent the schematic drawing of the cross-sectional view of the device.[24]

the micro-fabricated device. The optical microscope image of the typical Hall device with the equivalent circuit is shown in Fig. 2. In this device, the Pt buffer layer and the FM layer acted as the bottom and the top electrodes, respectively. In this setup, the electric field was applied across the Cr_2O_3 layer. The positive directions of magnetic and electric fields were defined as the direction from the bottom electrode to the top electrode. For the identical device used for the AHE measurements, the leakage current was also evaluated. At 312 K and 2000 kV/cm, the leakage current was the order of 1 A/cm^2 which is sufficiently low to rule out the current-induced switching.

Fig. 3(a) shows the AHE loops after the MEFC. Note that the AHE loops were measured at the highest magnetic field H of ±2 kOe and zero electric field E, and thus the AFM domain switching cannot occur during the AHE measurements. The negative exchange bias was observed for both the FC process with H = +10 kOe (black dotted) and the MEFC process with H = +10 kOe and E = −1000 kV/cm (gray solid).[24] Considering that Co and Cr spins are antiferromagnetically coupled at the interface,[36] the positive magnetic field favors the upward Co moment and the downward interfacial Cr moment. Since the interfacial Cr moment, i.e., as the boundary magnetization couples with the AFM order parameter, a negative EH also favors the downward Cr moment. Consequently, when $EH \leq 0$, the above-mentioned energy competition, and thus the switching of the exchange bias polarity, does not occur. However, when a positive EH was applied, the upward interfacial Cr moment is energetically favorable. When the value of EH is high enough to overcome the interfacial exchange coupling, the interfacial Cr moment should be upward, consequently leading to a positive exchange bias. As shown by the black solid line in Fig. 3(a), the AHE loop after the MEFC with H = +10 kOe and E = +1200 kV/cm represents the positive exchange bias, which agrees with the above-mentioned arguments.

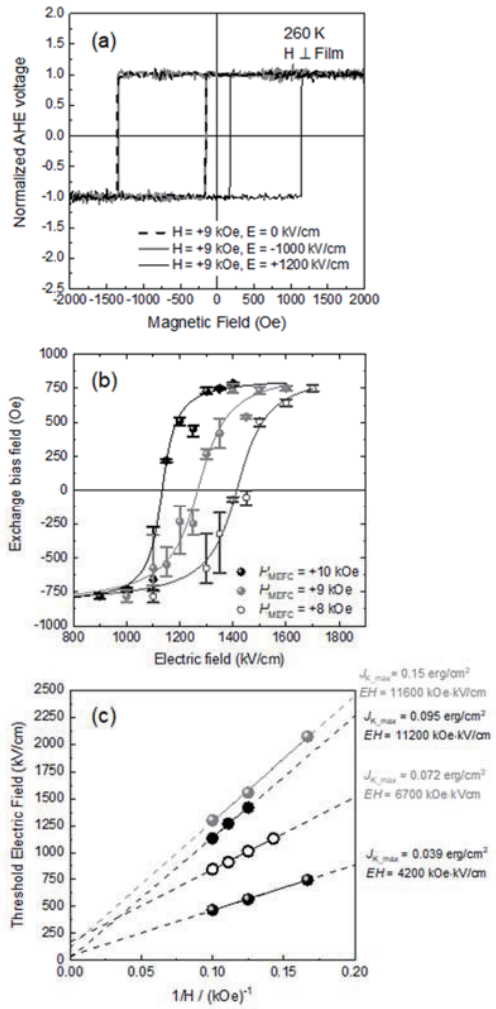

Fig. 3 (a) Typical AHE loops after MEFC with positive (gray dotted) and negative (black solid) EH field.[24] Film used was the Pt/Co/Pt/Cr_2O_3/Pt film. (b) Change in the exchange bias field with applied E during the MEFC for the Pt/Co/Cr_2O_3/Pt film. The applied H during the MEFC wss +10 kOe (black, closed circle), +9 kOe (gray, closed circle), and +8kOe (black, open circle).[30] (c) Change in E_{th} with the inverse H for some films with different J_K.[30]

As long as the exchange bias polarity is determined by the energy competition, there should be a threshold condition to switch the exchange bias polarity. Fig. 3(b) shows the change in the exchange bias field H_{EX} with respect to the electric field E during the MEFC with a constant magnetic field H. The sign of the exchange bias changes from negative to positive with increasing E. The change in H_{EX} with E can be represented by the functional form of $\tanh(\Delta G)$, where ΔG represents the energy difference between negative and positive exchange-biased states. This agrees with the previous energetic interpretation to induce the positive exchange bias in Fe/FeF_2 system by using the conventional FC process in which the energy competition between the interfacial exchange coupling and Zeeman energy in FeF_2 layer was considered.[37] This analogy can be understood through eq. (2), which represents the Zeeman energy of the E-induced magnetization ($\alpha_{ij}E$) based on the magnetic field H.

When defining the threshold electric field E_{th} at which the exchange bias is zero, E_{th} increases with decreasing H during the MEFC. As shown in Fig. 3(c), E_{th} is inversely proportional to H, as shown by eq. (2). The slope of the E_{th}–1/H relationship yields the required EH product to switch the exchange bias polarity, $(EH)_{th}$. According to the above-mentioned arguments, the $(EH)_{th}$ value increases with the interfacial exchange coupling. Although the direct determination of the interfacial exchange coupling energy is difficult, J_K is a measure of the exchange coupling energy. Fig. 3(c) shows the E_{th}–1/H relationship for some films with different J_K values.[31] The slope of the curve increases with J_K, thus supporting the earlier discussion.

2.2 Isothermal process

Although the switching based on the MEFC process requires temperature hysteresis, the temperature change is not involved in the isothermal switching. In addition, we can obtain additional information, such as the reversibility of the switching[27] and the dynamics of the ME-induced switching[28], which could help with the full understanding of ME switching. This section presents the results for the Pt/Co/Au/Cr_2O_3/Pt stacked film, in which the Au spacer layer was deposited to tune the interfacial exchange coupling strength and interfacial magnetic anisotropy[30].

2.2.1 Static switching using DC voltage

First, we discuss the reversible switching of the perpendicular exchange bias. Iyama and Kimura[39] reported that Cr_2O_3 showed a clear hysteresis in both the M–H curve under constant electric field E and the P–E curve under constant magnetic field H: a ferromagnetic (ferroelectric) feature under constant $E(H)$. This implies that the magnetic domain state of Cr_2O_3 is switchable in an isothermal manner. As the exchange bias polarity couples with the AFM domain state through boundary magnetization, hysteresis also occurs with the change in H_{EX} and E under constant H, as shown in Fig. 3(a). This is contrastive to the MEFC process in which the interfacial Cr^{3+} orientation is affected by the above-mentioned energy competition. We obtained different E_{th} values of H_{EX} for the positive-to-negative (P-to-N) and the negative-to-positive (N-to-P) switchings. The difference in E_{th} should be due to the unidirectional nature of the interfacial exchange coupling at the FM/AFM interface. The sign of the switching direction denotes the exchange bias polarity. Here, we discuss the energy condition of the isothermal switching. The magnetic free energy of the oppositely directed AFM domains per unit area for the FM/Cr_2O_3 exchange-coupled system can be expressed as

$$\begin{aligned} F &= K_{AFM} t_{AFM} \sin^2\theta - \alpha_{33} E H t_{AFM} \cos\theta \\ &\quad - M_{AFM} H \cos\theta - J S_{FM} S_{AFM} \cos\theta \\ &= K_{AFM} t_{AFM} \sin^2\theta \\ &\quad - \left(\alpha_{33} E t_{AFM} + M_{AFM}\right) H \cos\theta \\ &\quad - J S_{FM} S_{AFM} \cos\theta \end{aligned} \tag{3}$$

where K_{AFM} is the magnetic anisotropy energy density of the AFM layer, t_{AFM} is the AFM layer thickness, α_{33} is the ME coefficient, J is the interfacial exchange coupling energy, S_{FM} and S_{AFM} are the FM and AFM spins, respectively, and M_{AFM} is the uncompensated AFM moment. Further, θ is denoted by the angle between the interfacial AFM and FM spins (or H). The first, second, and third terms represent the magnetic anisotropy energy, Zeeman energy of the E-induced magnetization and uncompensated AFM spin, and the interfacial exchange coupling, respectively. M_{AFM} can be caused by the defect-induced finite magnetization[40] and/or the interfacial uncompensated AFM moment, which was the dominant factor in our case.[27] Note that in eq. (3), the FM spins are fixed to the direction of magnetic field H because the applied magnetic field H during the application of electric field E is high enough (> 40 kOe) to fix the FM spin. Thus, the Zeeman energy and magnetic anisotropy energy of the FM layer are not included in eq. (3) because these terms become constant when the FM magnetization is fixed. By minimizing eq. (3), the energy condition for ME switching is derived as[27]

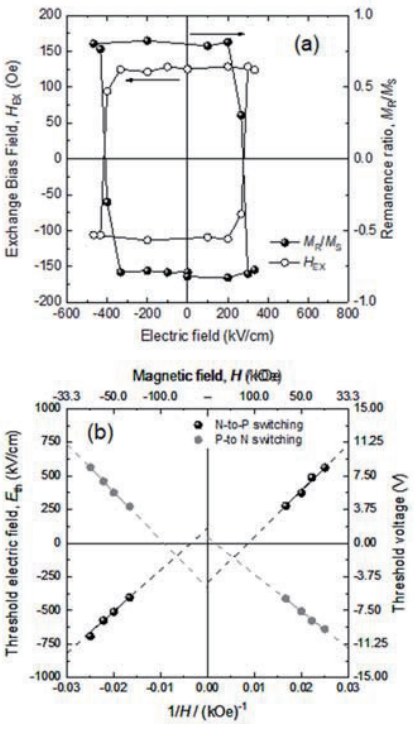

Fig. 4 (a) Changes of H_{EX} (left axis) and M_R/M_S(right axis) with E measured at 280 K. (b) Change of E_{th} as a function of $1/H$ for both N-to-P (solid) and P-to-N (open) switchings.[27]

$$\left(\alpha_{33} E + \frac{M_{AFM}}{t_{AFM}}\right) H = \pm 2K_{AFM} - \frac{J S_{FM} S_{AFM}}{t_{AFM}} \tag{4}$$

Each sign of the first term corresponds to the N-to-P and P-to-N switchings. Fig. 3(b) shows the magnetic field dependence of E_{th}, which is inversely proportional to H, as shown in eq. (4).

The unique feature that appeared in the all-thin-film system was (1) the different switching energy depending on the switching direction and (2) the appearance of the offset E in the E-$1/H$ relationship. The former is found in the difference in the slope of two curves, i.e. N-to-P switching and P-to-N switching. Accordingly, the slopes of the two curves give K_{AFM} and $JS_{FM}S_{AFM}$, whose values are 4.5±0.6 $\times 10^3$ J/m^3 and 1.5±0.2 $\times 10^{-2}$ mJ/m^2, respectively, assuming α_{33} = 3–4 ps/m. The estimated K_{AFM} is approximately half of the K_{AFM} of the bulk Cr_2O_3 at the measurement temperature of 280 K. This underestimation is probably because the above-mentioned estimation assumes the coherent rotation, while in reality, the nucleation and propagation of the reversed AFM domains should be involved[26]. In addition, the estimated value of $JS_{FM}S_{AFM}$ differs from that of the ideal model. That is, the estimated $JS_{FM}S_{AFM}$ was

approximately twice of the exchange anisotropy energy density, $J_K = H_{EX} \cdot M_S \cdot t_{FM} = 5.8 \times 10^{-3}$ mJ/m^2. The values of $JS_{FM}S_{AFM}$ and J_K might be equal when the pinned spin model[41] is valid in our film. However, in actuality, the interfacial Cr moments were not perfectly pinned but canted from the original direction with respect to the FM magnetization reversal,[36] which obviously deviates from the pinned spin model.

The offset E in the E-$1/H$ relationship, i.e., the nonzero E_{th} interception in the limit of $1/H$ to zero is another characteristics of all-thin-film system. According to eq. (3), the offset E_{th} is caused by the uncompensated AFM moment M_{AFM}. In our system, M_{AFM} relevant to the offset E_{th} is mainly the interfacial uncompensated AFM moment. This should be reasonable because the ME switching of the AFM domain detected through the exchange bias is an interfacial effect. In other words, by utilizing E_0 positively, the shift of the E-$1/H$ curve from the origin becomes significant. In the practical use, E_{th} at the certain H decreases with increasing E_0, i.e increasing M_{AFM}[40,42] or decreasing t_{AFM} which may become one solution to decrease the switching energy.

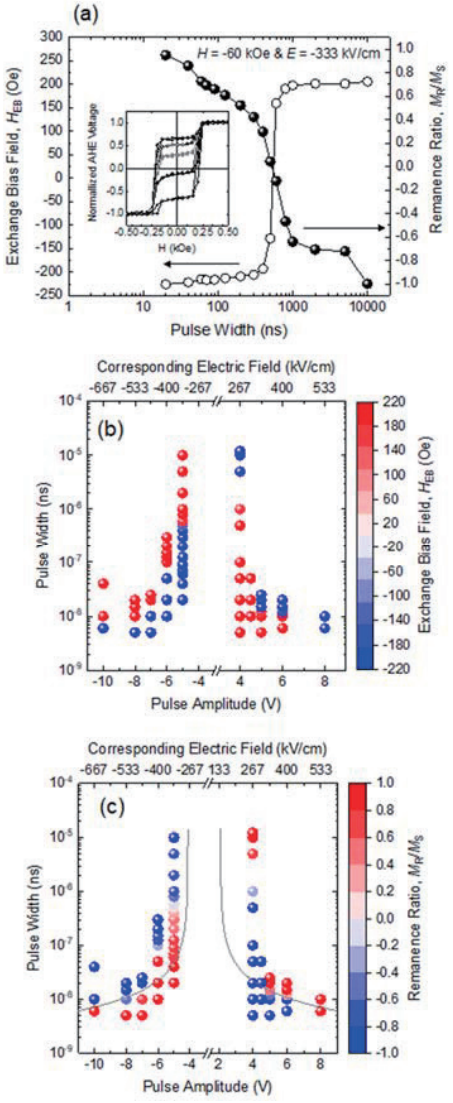

Fig. 5 (a) Changes in H_{EX} and M_R/M_S as a function of pulse width. H_{EX} and M_R/M_S were collected from the AHE loops after applying pulsed E under the constant H (= –60 kOe). The pulse amplitude was –333 kV/cm. Inset of (a) represents the typical AHE loop at the intermediate state. Changes in (b) H_{EX} and (c) M_R/M_S as functions of pulse amplitude and width, with white/black circles representing positive/negative values and their color depth representing absolute values. Solid line in (c) represents the calculated switching time. Measurement temperature was 280 K.[28]

2.2.2 Dynamical switching using pulse voltage

The important advantage of isothermal switching is that we can access the switching dynamics by adopting the pulsed magnetic or electric fields. In general, the pulse width of the pulsed magnetic field above several tens of kOe is in the range of milliseconds.[43] In contrast, the fast pulse E below microseconds can be easily generated using the general pulse generator. Thus, we can access fast dynamics by adopting the pulsed electric field and a constant magnetic field. Figure 4(a) shows the change in H_{EX} and M_R/M_S as a function of pulse width; these factors were collected from the AHE loops after applying H = –60 kOe and pulsed electric field with the amplitude of –333 kV/cm and width of 20 ns–10 μs.[28] As the DC E_{th} value of this film was –275 kV/cm (–4.1 V; see reference 28), the above-mentioned condition is slightly above the DC threshold condition. With increasing pulse width, H_{EX} (M_R/M_S) changes from negative (positive) to positive (negative) at the pulse width of 500 ns. The change in M_R/M_S is gradual compared with that in H_{EX}. This is because the coercivity H_C is lower than H_{EX}, the magnetization reversal is sharp around H_C, and the two-step magnetization process was observed at the intermediate state, as shows in the inset of Fig. 4(a). The slow switching time suggests that the switching process is dominated by the domain wall motion. In such a case, the switching time is dominated by the domain wall velocity and could be decreased by increasing the pulse amplitude. Figures 4(b) and 4(c) show the change of H_{EX} and M_R/M_S as functions of pulse amplitude and pulse width, respectively. The magnetic field during the application of an electric field was maintained at –60 kOe. The switching time decreases with increasing pulse amplitude, as expected earlier. As the ME-induced switching is triggered by the electric field, the microscopic origin of the domain wall motion might be different from the magnetic-field induced domain wall dynamics observed in the ordinal FM layer.[44–46] Nonetheless, as indicated by eqs. (1) and (2), the role of electric field E is to induce magnetization, and a change in E alters the energy gain by the Zeeman energy of the E-induced magnetization. Therefore, the driving force to induce the magnetic domain wall propagation should be analogous to the case of FM (or ferrimagnetic) domain wall. By assuming that Cr_2O_3 under a finite E behaves as a ferrimagnet,[32] the domain wall velocity was calculated based on the simple theory discussed in refs. 44–47. The details of the calculation can be found in ref. 28. As shown by the solid line in Fig. 4(c), the switching time can be roughly reproduced using the simple model with some assumed values: domain wall width, 38 nm[48]; ME

coefficient at 280 K, 3.5 ps/m[49]; Ginbert damping parameter of each sublattice, 0.05; and travel distance, 1 μm (half of the Hall device width). Despite the rough agreement in the switching times, some assumed values need further investigation. For instance, the assumed Gilbert damping parameter of each sublattice is the order of 10^{-2}–10^{-1}, which may be larger than the predicted value.[48] One reason may be the creep motion of the domain wall under our adopted experimental condition as indicated by the large deviation in the low amplitude regime. The direct observation of the ME-induced magnetization reversal process is beneficial for both the quantitative analysis and deeper understanding of the phenomena.

3. Element-specific magnetic domain observation

For the observation of the ME-induced magnetization switching process, it can be simply assumed that FM and AFM domains are coupled spatially, at least, at the remanent state. In other words, if this assumption is valid, we can obtain the AFM domain pattern by observing the FM domain. However, this is nontrivial. In the case of the in-plane exchange-biased film, the AFM domains can be imaged through X-ray linear dichroism (XMLD).[50,51] Accordingly, the AFM domain just below the individual FM domains is not a single domain state, implying that FM and AFM domain patterns are not the same. Hence, as a first step in the investigation, the magnetic domain states of FM and AFM layers must be obtained independently.

The XMLD technique is not applicable for our system because the AFM spin orientation should be restricted to upward or downward directions (see Fig. 1), and such collinear spins are not distinguishable through XMLD. X-ray magnetic circular dichroism (XMCD) complements this limitation and is a powerful tool for the perpendicularly directed spin system. Based on the XMCD measurements by using the focused soft X-ray, we observed the spatial distribution of the XMCD intensity corresponding to the magnetic domains for FM Co and AFM Cr spins independently.[33] In this work, we employed the scanning XMCD microscope equipped at BL25SU, SPring-8. The schematic drawing of the scanning XCMD microscope is shown in Fig. 6. In this microscope, the soft X-ray was focused on the sample using the Fresnel Zone Plate (FZP) and the order sorting aperture (OSA). By scanning the sample in x and y directions in keeping the focused state, the special distribution of the XMCD intensity was collected. In this microscope, the XMCD signal can be detected based on the surface-sensitive total electron yield method, suitable to detect the tiny signal from the interfacial uncompensated Cr spin. The details of this microscope can be found in refs. 33 and 52.

Figure 7shows the spatial distributions of XMCD of Co and Cr for the Pt/Co/Cr_2O_3/Pt thin film measured at 205 K. The multidomain state was created through AC-demagnetization at room temperature, and then the

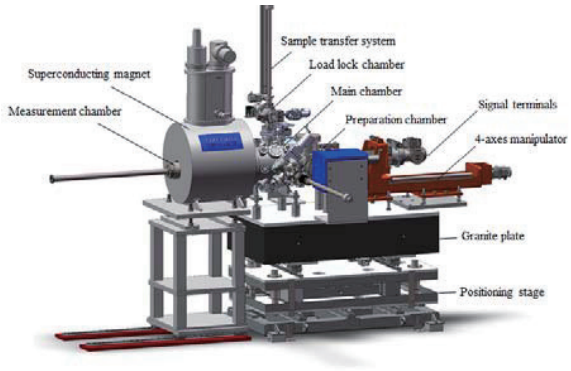

Fig. 6 Schematic drawings of the scanning XMCD microscope.[Courtesy to Dr. Nakamura and Dr. Kotani of JASRI] Details about the optical setup, the scanning method et al should be referred to ref. 52.

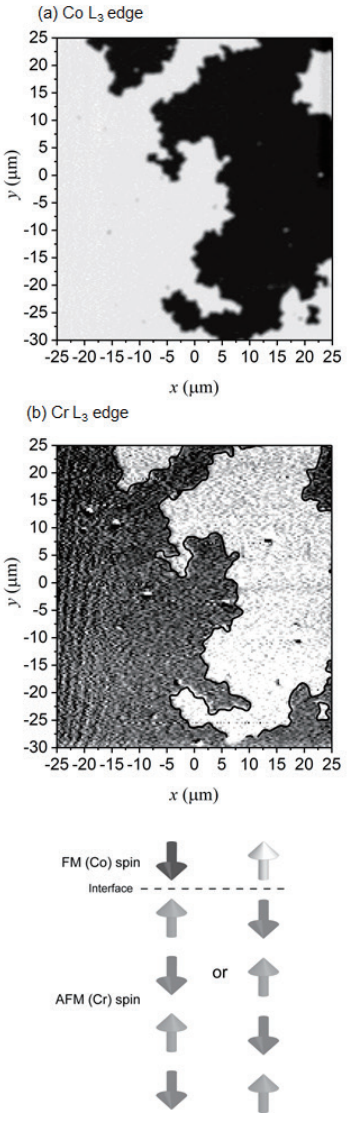

Fig. 7 Spatial distribution of XMCD measured at 205 K. Photon energy used for the imaging was (a) 778 eV (Co L_3 edge) and (b) 576 eV (Cr L_3 edge). Colors correspond to spin orientations schematically shown at bottom. Black solid line in (b) represents the domain boundary of the oppositely directed FM domains [33]

sample was cooled to retain the demagnetized state. Note that the XMCD from the Cr was performed using the interfacial uncompensated Cr moment. Two patterns were observed to be very similar indicating that the FM and AFM domains are spatially coupled. This spatial coupling of the magnetic domains is probably due to the strong interfacial exchange coupling and the collinear interfacial spin alignments of both Co and Cr. The sign of the XMCD is contradictory for Co and Cr indicating antiferromagnetic interfacial exchange coupling.[36] From the spatial coupling of the magnetic domains, the exchange bias polarity can be assumed to be determined according to the domain-by-domain basis, implying that the exchange bias polarity is determined by the interfacial AFM moments, i.e., the boundary magnetization. This can be directly verified by measuring the local magnetization curve on the individual magnetic domains; this is under investigation. For the direct observation of the ME-induced magnetization switching process, in addition to the imaging technique described previously, the applications of magnetic field above several tens of kOe and the electric field (of both DC and pulse) in the microscope instrument are necessary. These techniques are now in the developing stage and will be reported in the near future.

4. Summary

In this article, we reviewed the ME-induced magnetization reversal mainly based on our own results. Discovered in the 1950s in bulk Cr_2O_3, the ME effect was recently observed in an all-thin-film system. Owing of this development, we could address the various phenomena involving the ME effect, e.g., the control of the interfacial magnetization and switching dynamics. Many challenges still exist for the actual application of the ME effect to a storage/memory device, e.g., the reduction of the switching energy, fast switching, and thermal stability. To solve these challenges, a deeper understanding of the ME-induced phenomena is essential.

Acknowledgements Part of this work was conducted by collaborating with Dr. Tetsuya Nakamura, Dr. Motohiro Suzuki, Dr. Yoshinori Kotani, Dr. Kentaro Toyoki (JASRI), Dr. Chiharu Mitsumata (NIMS), Dr. Tatsuo Shibata, and Dr. Shogo Yonemura (TDK corp.). This work was partly supported by JSPS KAKENHI (Grant Nos. 16H03832, 16H02389), the ImPACT program of Council for Science, Technology and Innovation (Cabinet Office, Government of Japan), and the Photonics Advanced Research Center (PARC) at Osaka University.

References

1) P. Curie: *J. Phys. (Paris)*, **3**, 393 (1894).
2) A. Perrier: *Arch. Sci. Phys. Nat.*, 4, 369 (1922).
3) A. Perrier and A. J. Starling: *Arch. Sci. Phys. Nat.*, **4**, 373 (1922), *ibid*, **5**, 333 (1923).
4) A. Perrier and C. E. Borel: *Arch. Sci. Phys. Nat.*, **7**, 289 (1925).
5) A. Piccard: *Arch. Sci. Phys. Nat.*, **6**, 404 (1924).
6) P. Debye: *Z. Phys.*, **36**, 300 (1926).
7) J. H. Van Vleck: *The theory of electric and magneto susceptibilities* (Oxford University Press, London, 1932), pp.113-121 and pp. 279-281.
8) L. D. Landau and E. M. Lifshitz, *Electrodynamics of continuous media* (English Transl. Pregamon Press, Oxford, 1960), p. 115, p.119, pp.313-344.
9) I. E. Dzyaloshinskii: *Sov. Phys. JETP*, **10**, 628 (1959).
10) D. N. Astrov: Sov. *Phys. JETP*, **11**, 708 (1960).
11) V. J. Folen, G. T. Rado, and E. W. Stadler: *Phys. Rev. Lett.*, **6**, 607 (1961).
12) T. Arima: *J. Phys. Soc. Jpn.*, **80**, 052001 (2011).
13) T. H. O'Dell, *The electrodynamics of magneto-electric media* (North-Holland Publishing Company, 1970), Chapter 1.
14) M. Fiebig: *J. Phys. D: Appl. Phys.*, **38**, R123 (2005).
15) P. Borisov, A. Hochstrat, X. Chen, W. Kleemann, and C. Binek: *Phys. Rev. Lett.*, **94**, 117203 (2005).
16) J. Nogués and I. K. Schuller, *J. Magn. Magn. Mater.*, **192**, 203 (1999).
17) A. E. Berkowitz and K. Takano: *J. Magn. Magn. Mater.*, **200**, 553 (2000).
18) R. L. Stamps: *J. Phys. D: Appl. Phys.*, **33**, R247 (2000).
19) X. He, Y. Wang, A. N. Caruso, E. Voscovo, K. D. Bealshchenko, P. A. Dowben, and C. Binek: *Nat. Mater.*, **9**, 579 (2010).
20) A. F. Andreev, JETP Lett., **63**, 758 (1996).
21) K. D. Belashchenko: *Phys. Rev. Lett.*, **105**, 147204 (2010).
22) K. Toyoki, Y. Shiratsuchi, T. Nakamura, C. Mitsumata, S. Harimoto, Y. Takechi, T. Nishimura, H. Nomura, and R. Nakatani: *Appl. Phys. Express*, **7**, 114201 (2014).
23) T. Ashida, M. Oisa, N. Shimomura, T. Nozakim T. Shibata, and M. Sahashi: *Appl. Phys. Lett.*, **104**, 152409 (2014).
24) K. Toyoki, Y. Shiratsuchi, A. Kobane, S. Harimoto, S. Onoue, H. Nomura, and R. Nakatani: *J. Appl. Phys.*, **117**, 19D902 (2015).
25) T. Ashida, M. Oida, N. Shimomura, T. Nozaki, T. Shibata, and M. Sahashi: *Appl. Phys. Lett.*, **106**, 132407 (2015).
26) K. Toyoki, Y. Shiratsuchi, A. Kobane, C. Mitsumata, Y. Kotani, T. Nakamura, and R. Nakatani: *Appl. Phys. Lett.*, **106**, 162494 (2015).
27) T. V. A. Nguyen, Y. Shiratsuchi, A. Kobane, S. Yoshida, and R. Nakatani: *J. Appl. Phys.*, 122, 073905 (2017).
28) T. V. A. Nguyen, Y. Shiratsuchi, and R. Nakatani: *Appl. Phys. Express*, **10**, 083002 (2017).
29) Y. Shiratsuchi, Y. Nakano, N. Inami, T. Ueno, K. Ono, R. Kumai, R. Sagayama, and R. Nakatani: *J. Appl. Phys.*, **123**, 103903 (2018).
30) Y. Shiratsuchi, W. Kuroda, T. V. A. Nguyen, Y. Kotani, K. Toyoki, T. Nakamura, M. Suzuki, K. Nakamura, and R. Nakatani: *J. Appl. Phys.*, **121**, 073902 (2017).
31) Y. Shiratsuchi, and R. Nakatani: *Mater. Trans.*, **57**, 781 (2016).
32) T. J. Martin, and J. C. Anderson: *IEEE Trans. Magn.*, **2**, 446 (1966).
33) Y. Shiratsuchi, Y. Kotani, S. Yoshida, Y. Yoshikawa, K. Toyoki, A. Kobane, R. Nakatani, and T. Nakamura: *AIMS Mater. Sci.*, **2**, 484 (2015).
34) Y. Shiratsuchi, S. Watanabe, H. Yoshida, N. Kishida, R. Nakatani, Y. Kotani, K. Toyoki, and T. Nakamura: to be submitted.
35) T. G. MacGuire, E. J .Scott, and F. H. Grannis: *Phys. Rev.*, **102**, 1000 (1956).
36) Y. Shiratsuchi, H. Noutomi, H. Oikawa, T. Nakamura, M. Suzuki, T. Fujita, K. Arakawa, Y. Takechi, H. Mori, T. Kinoshita, M. Yamamoto, and R. Nakatani: *Phys. Rev. Lett.*, **109**, 077202 (2012).
37) B. Kagerer, Ch. Binek, and W. Kleemann: *J. Magn. Magn. Mater.*, **217**, 139 (2000).
38) K. Toyoki, Y. Shiratsuchi, A. Kobane, S. Harimoto, S. Onoue, H. Nomura, and R. Nakatani: *J. Appl. Phys.*, **117**, 19D902

(2015).
39) A. Iyama, and T. Kimura: *Phys. Rev. B*, **87**, 180408(R) (2013).
40) T. Kosub, M. Kopte, R. Hühne, P. Appel, B. Shields, P. Maletinsky, R. Hübner, M. O. Liedke, J. Fassbender, O. G. Schmidt, and D. Makarov: *Nat. Comm.*, **8**, 13985 (2017).
41) W. H. Meiklejohn, and C. P. Bean: *Phys. Rev.*, **102**, 1413 (1956), *ibid* **105**, 904 (1957).
42) M. Al-Mahdawi, S. P. Pati, Y. Shiokawa, S. Ye, T. Nozaki, and M. Sahashi; *Phys. Rev. B*, **95**, 144423 (2017).
43) T. Nakamura, Y. Narumi, T. Hirono, M. Hayashi, K. Kodama, M. Tsunoda, S. Isogami, H. Takahashi, T. Kinoshita, K. Kindo, and H. Nojiri: *Appl. Phys. Express*, **4**, 066602 (2011).
44) T. Ono, H. Miyajima, J. Shigeto, N. Hosoito, and T. Shinjo: *Science*, **284**, 468 (1999).
45) D. Atkinson, D. A. Allwood, G. X. Cooke, C. C. Faulkner, and R. D. Cowburn: *Nat. Mater.*, **2**, 85 (2003).
46) G. D. Beach, C. Nistor, K. Maxim, and J. K. Erskine: *Nat. Mater.*, **4**, 741 (2005).
47) R. Giles, and M. Mascuripur: *J. Mag. Soc. Jpn.*, **15**, 299 (1991).
48) K. D. Belashchenko, O. Tedemyshyov, A. A. Kovalev, and O. A. Tretiakov: *Appl. Phys. Lett.*, **108**, 132403 (2016).
49) P. Borisov, T. Ashida, T. Nozaki, M. Sahashi, and D. Lederman: *Phys. Rev. B*, **93**, 174415 (2016).
50) A. Scholl, J. Stöhr, J. Lüning, J. W. Seo, J. Frompeyrine, H. Siegwart, J. –P. Locquet, F. Nolting, S. Anders, E. E. Fullerton, M. R. Scheinfein, and H. A. Padmore: *Science*, **287**, 1014 (2000).
51) F. Nolting, A. Scholl, J. Stöhr, J. W. Seo, J. FOmpeyrfine, H. Siegwark, J. –P. Locquet, S. Anders, J. Lüning, E. E. Fulelrton, M. F. Toney, M. R. Scheinfein, and H. A. Padmore: *Nature*, **405**, 767 (2000).
52) Y. Kotani, Y. Senba, K. Toyoki, D. Bikkington, H. Okazaki, A. Yasui, W. Ueno, H. Ohashi, S. Hirosawa, Y. Shiratsuchi, and T. Nakamura: *J. Synchrotron Rad.*, **25** in press. https://doi.org/10.1107/S1600577518009177.

Received Apr. 30, 2018. Accepted Jul. 24, 2018.

J. Magn. Soc. Jpn., **42**, 127-137 (2018)

<Paper>

Understanding Signal-to-Noise Ratio in Heat-Assisted Magnetic Recording

T. Kobayashi, Y. Nakatani*, and Y. Fujiwara

Graduate School of Engineering, Mie Univ., *1577 Kurimamachiya-cho, Tsu 514-8507, Japan*

*Graduate School of Informatics and Engineering, Univ. of Electro-Communications, *1-5-1 Chofugaoka, Chofu 182-8585, Japan*

We improve our model calculation for heat-assisted magnetic recording (HAMR) considering the temperature dependence of the attempt frequency. Then, the signal-to-noise ratio dependence on writing field is calculated for various calculation parameters by employing both our model calculation and the conventionally used micromagnetic calculation. The tendencies of the results of our model calculation and of the micromagnetic calculation are almost the same by this improvement. Therefore, our model calculation can be used for HAMR design. The writing process can be described using the temperature dependences of the grain magnetization reversal probability and the attempt number. If the Gilbert damping constant is small, writing is difficult since the attempt number is small. Write-error can be reduced by reducing the linear velocity, and erasure-after-write can be reduced by increasing the thermal gradient and/or the grain column number.

Key words: heat-assisted magnetic recording, signal-to-noise ratio, grain magnetization reversal probability, attempt number

1. Introduction

Heat-assisted magnetic recording (HAMR) is a promising candidate as a next generation magnetic recording method beyond the trilemma limit[1].

We have already proposed a new HAMR model calculation[2),3)]. The grain magnetization reversal probability and the attempt period, whose inverse is the attempt frequency f_0, are key physical quantities in our model calculation. We used a constant f_0 value in our previous model calculation. We have also calculated the temperature dependence of f_0 [4)] employing the conventionally used micromagnetic calculation.

In this study, we improve our model calculation considering the temperature dependence of f_0. Then, we calculate the dependence of the signal-to-noise ratio (SNR) on the writing field for various calculation parameters in HAMR. And we compare the results with those calculated employing the conventionally used micromagnetic calculation at the same time to determine whether our model calculation can be used for HAMR design. Furthermore, we provide the SNR results with physical implications employing our model calculation with a view to HAMR design.

2. Calculation Method

2.1 Calculation conditions

The medium was assumed to be granular. The writing field switching timing and the calculation conditions are summarized in Fig. 1 (a). The mean grain size D_m, the standard deviation of the grain size σ_D / D_m, and the grain height h were 4.9 nm, 10 %, and 8 nm, respectively, and so the grain volume V_m for D_m was $D_m \times D_m \times h$ = 193 nm^3. The Curie temperature T_c and the standard deviation of the Curie temperature σ_{Tc} / T_c were 700 K and 0 %, respectively, since a higher anisotropy constant ratio K_u / K_{bulk} is necessary if T_c is low[5)] where K_u / K_{bulk} is the intrinsic ratio of the medium anisotropy constant K_u to bulk FePt K_u [6)]. The K_u / K_{bulk} value of the medium was 0.4. The calculation parameters were the bit pitch D_{BP}, the Gilbert damping constant α, the thermal gradient $\partial T / \partial x$ for the down-track direction, and the linear velocity v.

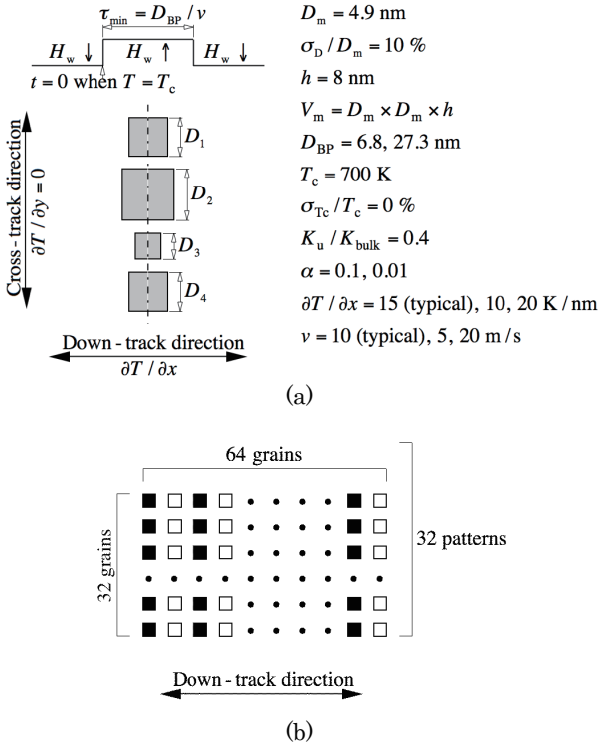

Fig. 1 (a) Writing field switching timing and calculation conditions, and (b) grain arrangement for signal-to-noise ratio calculation.

We used the damping constants α = 0.1 and 0.01 since the value of α just below T_c is unknown. Typical values were $\partial T/\partial y$ = 15 K/nm and v = 10 m/s. The thermal gradient $\partial T/\partial y$ for the cross-track direction was assumed to be 0 K/nm.

H_w and $\tau_{min} = D_{BP}/v$ are the writing field and the time available for writing each bit, respectively. The H_w direction is upward when time t is $2n\tau_{min} \le t < (2n+1)\tau_{min}$, and downward when $(2n+1)\tau_{min} \le t < (2n+2)\tau_{min}$ where n is an integer. When $t = n\tau_{min}$, the writing grain temperature T becomes T_c. There are fluctuations in the switching timing Δt and position Δx in a granular medium[3]. However, we assumed Δt = 0 and Δx = 0 in our discussion of the intrinsic phenomenon.

Figure 1 (b) shows the grain arrangement for the signal-to-noise ratio (SNR) calculation. We used a pattern consisting of 32 grains for the cross-track direction and 64 grains for the down-track direction, and we used 32 patterns for the SNR calculation. One bit consisted of 32 × 1 or 32 × 4 grains, namely one or four grain columns per bit, and D_{BP} = 6.8 or 27.3 nm, respectively. An initial magnetization direction, namely upward or downward, is randomly decided.

2.2 Model calculation

The magnetization direction of the grains was calculated using the magnetization reversal probability for every attempt time in our model calculation[2)~4)].

The switching probability P_- for each attempt where the magnetization M_s and the writing field H_w change from antiparallel to parallel is expressed as

$$P_- = \exp\left(-K_{\beta-}\right). \tag{1}$$

On the other hand,

$$P_+ = \exp\left(-K_{\beta+}\right) \tag{2}$$

is the probability for each attempt where M_s and H_w change from parallel to antiparallel. In these equations,

$$K_{\beta-}(T, H_w) = \frac{K_u(T)V}{kT}\left(1 - \frac{H_w}{H_k(T)}\right)^2 \quad \left(H_k(T) \ge H_w\right),$$

$$K_{\beta-}(T, H_w) = 0 \quad \left(H_k(T) < H_w\right), \tag{3}$$

and

$$K_{\beta+}(T, H_w) = \frac{K_u(T)V}{kT}\left(1 + \frac{H_w}{H_k(T)}\right)^2, \tag{4}$$

where K_u, V, k, T, and $H_k = 2K_u/M_s$ are the anisotropy constant, the grain volume, the Boltzmann constant, temperature, and the anisotropy field, respectively.

The temperature dependence of M_s was determined employing a mean field analysis[7)], and that of K_u was assumed to be proportional to M_s^2 [8)]. The Curie temperature T_c can be adjusted by the Cu simple dilution of $(Fe_{0.5}Pt_{0.5})_{1-z}Cu_z$. $M_s(T_c, T)$ is a function of T_c and T. $M_s(T_c = 770\ \mathrm{K}, T = 300\ \mathrm{K})$ = 1000 emu/cm^3 was assumed. $K_u(T_c, K_u/K_{bulk}, T)$ is a function of T_c, the anisotropy constant ratio K_u/K_{bulk}, and T. $K_u(T_c = 770\ \mathrm{K}, K_u/K_{bulk} = 1, T = 300\ \mathrm{K})$ = 70 Merg/cm^3 was assumed. We used $M_s(T_c = 700\ \mathrm{K}, T)$ and $K_u(T_c = 700\ \mathrm{K}, K_u/K_{bulk} = 0.4, T)$ for the calculation in this paper.

On the other hand, the attempt time t_k, which falls within an attempt period τ_{AP}, is determined as follows. The inverse of the attempt period is an attempt frequency $f_0 = 1/\tau_{AP}$. We improve our model calculation considering the temperature dependence of f_0. We have determined the temperature dependence of f_0 [4)] employing a conventionally used micromagnetic calculation with the Landau-Lifshitz-Gilbert (LLG) equation[9)] where we calculated the temperature dependence of the magnetic properties used in the f_0 calculation with a mean field analysis. The results can be fitted using

$$f_0(T) = \frac{2\alpha}{1+\alpha^2} f_1 \sqrt{\frac{V}{V_m}} \sqrt{\frac{600}{T}} \frac{K_u(T)}{K_u(600\ \mathrm{K})} \tag{5}$$

in consideration of reference 10) where f_1 = 500 (ns)$^{-1}$, V_m = 193 nm^3, and $K_u(600\ \mathrm{K})$ = 8.0 Merg/cm^3. Since there was a very good linear relationship between f_0 and T, we used

$$f_0(T) = \frac{2a\alpha}{1+\alpha^2} \sqrt{\frac{V}{V_m}} \frac{K_u/K_{bulk}}{0.4}(T_c - T) \tag{6}$$

instead of Eq. (5) in our calculation where a = 5 (nsK)$^{-1}$. The f_0 value becomes zero at T_c as shown in Eq. (6).

We defined an initial time t_{ini1} at $T = T_{th}$ = 699 K, which is close to T_c = 700 K, using

$$t_{ini1} = \frac{T_c - T_{th}}{(\partial T/\partial x)v} \tag{7}$$

since $\tau_{AP} = 1/f_0$ diverges to infinity at $T = T_c$. The next initial time t_{ini2} can be calculated using the mean attempt period τ_{APm} from t_{ini1} to t_{ini2} expressed by

$$t_{ini2} - t_{ini1} = \tau_{APm} = \frac{1}{t_{ini2} - t_{ini1}} \int_{t_{ini1}}^{t_{ini2}} \tau_{AP}(t)dt\,. \tag{8}$$

We assumed that the first attempt time t_1 is randomly decided between t_{ini1} and t_{ini2}. And the attempt time t_{k+1} $(k \ge 1)$ is determined with the following recurrence formula:

$$t_{k+1} - t_k = \tau_{APm} = \frac{1}{t_{k+1} - t_k} \int_{t_k}^{t_{k+1}} \tau_{AP}(t)dt\,. \tag{9}$$

Figure 2 shows the time dependence of the grain magnetization reversal probability $P_\pm$ for $t_1 = t_{ini1}$ and $t_2 = t_{ini2}$. In this paper, figures of $P_\pm$ with time

are shown in the same format. The filled circles indicate the attempt times whose interval is the mean attempt period τ_{APm}. The f_0 value is low just below T_c as shown in Eq. (6), and then $\tau_{AP} = 1/f_0$ is long just after t = 0 since the time t = 0 corresponds to the writing grain temperature T becoming T_c. The temperature decreases with time, and τ_{AP} decreases accordingly. Therefore, τ_{APm} decreases with time.

The writing field was assumed to be spatially uniform, the direction was perpendicular to the medium plane, and the rise time was zero. Neither the demagnetizing nor the magnetostatic fields were considered during writing since they are negligibly small. The output signal, media noise, and media signal-to-noise ratio (SNR) were calculated using the sensitivity function[11] of a magnetoresistive head with an element width of 218 nm, a shield-to-shield distance of 15 nm, and a 4.0 nm head-medium spacing. The element width is the same as the cross-track width of the simulation region.

The calculation procedure is described below. First, the medium was characterized by T_c = 700 K, K_u/K_{bulk} = 0.4, and α. The grain temperature fell with time from T_c according to the thermal gradient $\partial T/\partial x$ along the down-track direction and the linear velocity v. The attempt times were calculated. The magnetic property and then $P_\pm$ were calculated by undertaking a mean field analysis for every attempt time. The magnetization direction can be determined by the Monte Carlo method for every attempt time. The SNR was obtained from the grain magnetization patterns as shown in Fig. 1 (b).

2.3 Micromagnetic calculation

We also calculated the SNR employing a micromagnetic calculation using the LLG equation and compared the results with those obtained employing our model calculation. The calculation conditions for the model calculation and the micromagnetic calculation were the same.

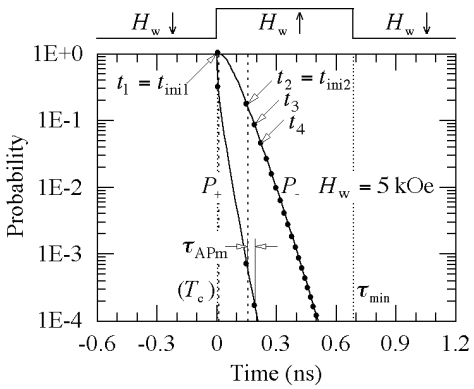

Fig. 2 Time dependence of grain magnetization reversal probability $P_\pm$ under conditions of 1 column/bit, damping constant α = 0.1, and typical values. The filled circles indicate the attempt times whose interval is the mean attempt period τ_{APm}.

3. Calculation Results

3.1 1 column/bit and α = 0.1

Representative grain magnetization patterns calculated employing our model are shown in Fig. 3 under the conditions of 1 column/bit, damping constant α = 0.1, and typical values. A writing field H_w of about 10 kOe is the best condition (see Fig. 6 (a)), H_w = 3 kOe is too small, and H_w = 17 kOe is too large.

Figure 4 shows the summation of the surface magnetic charge $M_{mn}D_{mn}^2$ for the cross-track direction m as a function of the position for the down-track direction n where M_{mn} and D_{mn} are the magnetization and the grain size for the grain arrangement matrix (m, n), respectively, the vertical axis is normalized by $32 \times M_s D_m^2$, and $M_{mn} = M_s$ since σ_{Tc}/T_c = 0. The surface charge summation is proportional to the signal amplitude read by the head with infinite resolution. The surface charge summations for Figs. 4 (a) and (c) are unsaturated according to the grain magnetization patterns for Figs. 3 (a) and (c), respectively.

This can be explained using the time dependence of the grain magnetization reversal probability P_- for various H_w values as shown in Fig. 5. Normal write-error (WE)[2] means that the magnetization does not switch to the recording direction, and WE occurs during writing ($0 \le t < \tau_{min}$). The attempt number is important when P_- is high. For H_w = 3 kOe, since the attempt number, that is, the filled circle number, is small when P_- is high, WE occurs. On the other hand, erasure-after-write (EAW)[2] is the grain magnetization reversal in the opposite direction to the recording direction caused by changing the H_w direction at the end of the writing time τ_{min}, and EAW occurs after writing ($t \ge \tau_{min}$). The P_- value is important at the end of the writing time τ_{min}. For H_w = 17 kOe, since the P_- value at τ_{min} designated by an open circle is not sufficiently low, EAW occurs. For H_w = 10 kOe, the attempt number is sufficiently large when P_- is high,

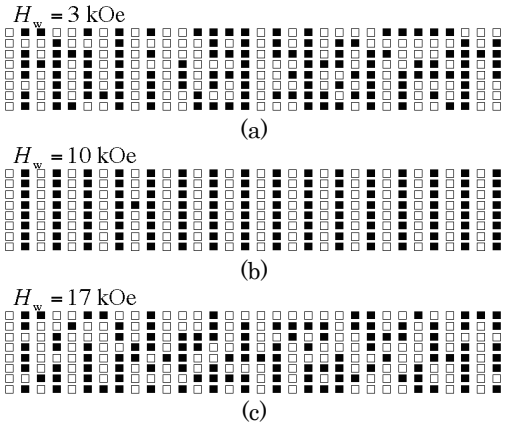

Fig. 3 Representative grain magnetization patterns for (a) writing field H_w = 3 kOe, (b) 10 kOe, and (c) 17 kOe under conditions of 1 column/bit, damping constant α = 0.1, and typical values.

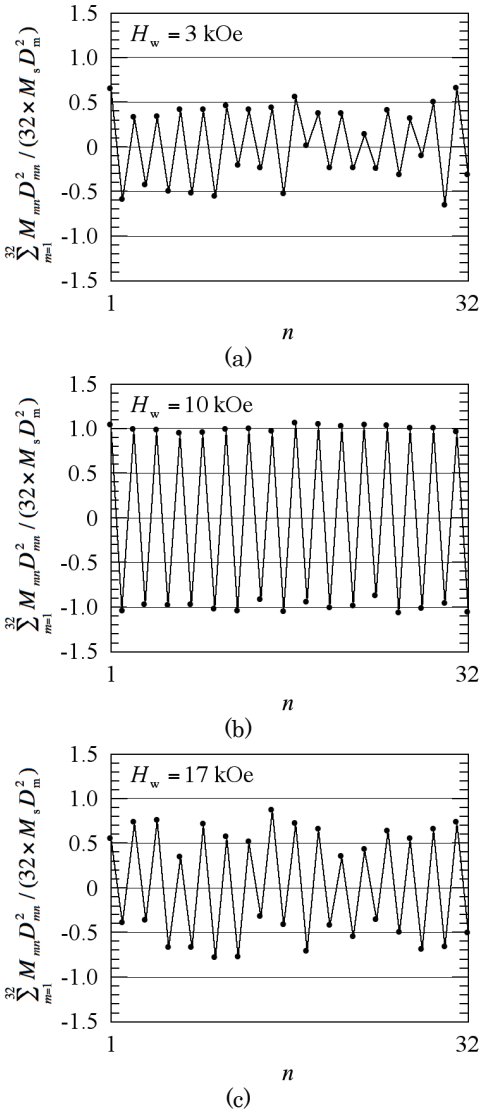

Fig. 4 Summation of surface magnetic charges $M_{mn}D_{mn}^2$ for cross-track direction m as a function of position for down-track direction n under conditions of 1 column/bit, α = 0.1, and typical values.

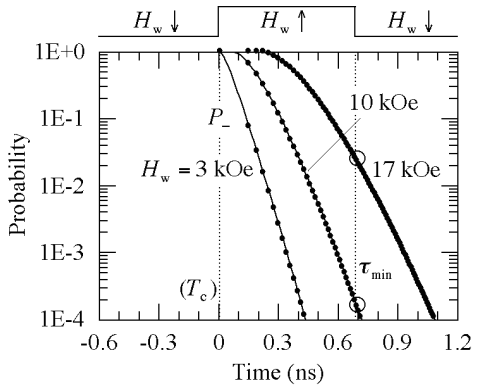

Fig. 5 Time dependence of grain magnetization reversal probability P_- for various H_w values under conditions of 1 column/bit, α = 0.1, and typical values.

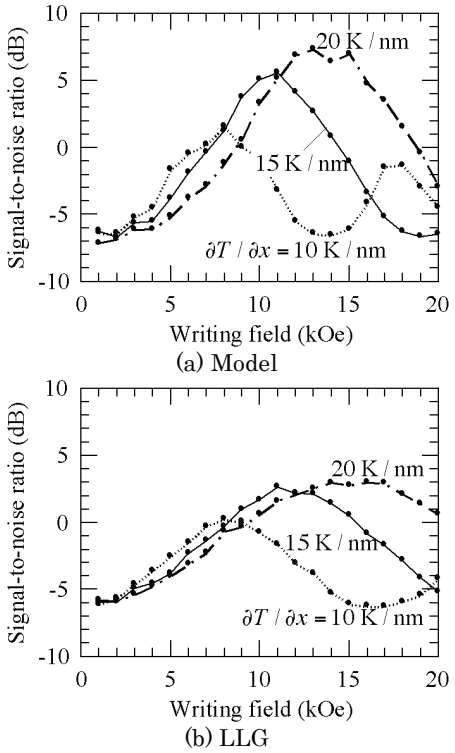

Fig. 6 Dependence of signal-to-noise ratio on writing field. (a) Model calculation and (b) micromagnetic (LLG) calculation for various thermal gradients $\partial T / \partial x$ under conditions of 1 column/bit, α = 0.1, and linear velocity v = 10 m/s.

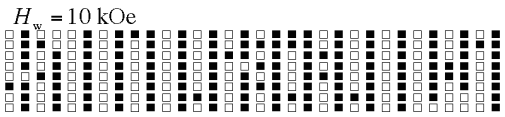

Fig. 7 Representative grain magnetization patterns calculated employing a micromagnetic calculation for writing field H_w = 10 kOe under conditions of 1 column/bit, damping constant α = 0.1, and typical values.

and the P_- value at τ_{min} designated by an open circle is sufficiently low. Therefore, both WE and EAW are low.

Figure 6 (a) shows the dependence of the signal-to-noise ratio (SNR) on the writing field H_w for various thermal gradients $\partial T / \partial x$ calculated employing our model. The increase in SNR as H_w increases in a low H_w region is caused by a reduction in WE since WE means that the magnetization does not switch to the recording direction during writing, and WE is caused by an insufficient H_w. The decrease in SNR as H_w increases in a high H_w region is caused by EAW since EAW is the magnetization reversal in the opposite direction to the recording direction after writing, and EAW is caused by an excessive H_w. The increase in SNR as H_w increases at more than about 14 kOe for $\partial T / \partial x$ = 10 K/nm in Fig. 6 (a) is caused by after-write (AW). AW occurs after writing ($t \geq \tau_{min}$).

Therefore, if the written data is “101010” for “write”, it is “010101” for “after-write”.

The results in Fig. 6 (a) can be compared with those in Fig. 6 (b), which were determined employing a micromagnetic calculation using the LLG equation. Although AW for $\partial T/\partial x$ = 10 K/nm in Fig. 6 (b) is underestimated, the tendencies are almost the same.

The maximum SNR value in Fig. 6 (b) is lower than that in Fig. 6 (a). This is attributed to the difference between the grain magnetization patterns in Fig. 7 and in Fig. 3 (b). There are many error grains in the grain pattern calculated employing a micromagnetic calculation for H_w = 10 kOe as shown in Fig. 7. The writing field at which the SNR value shows the maximum in Fig. 6 (b) is somewhat higher than that in Fig. 6 (a). This is attributed to the determination method of the attempt time in our model calculation described in **2.2**. In this way, although our model calculation is a coarse estimation, the tendencies of the results in Figs. 6 (a) and (b) are almost the same.

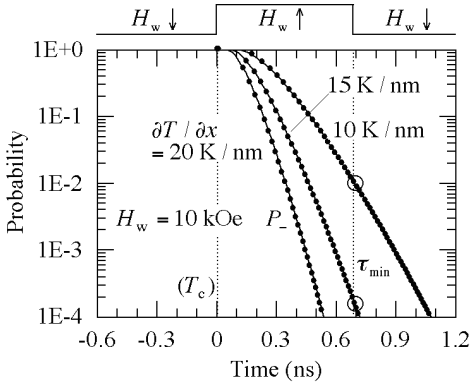

Fig. 8 Time dependence of grain magnetization reversal probability P_- for various $\partial T/\partial x$ values under conditions of 1 column/bit, α = 0.1, and v = 10 m/s.

A large dependence of EAW on $\partial T/\partial x$ can be seen in Fig. 6. Figure 8 shows the time dependence of grain reversal probability P_- for various thermal gradients $\partial T/\partial x$ at H_w = 10 kOe. The P_- values at τ_{min} designated by open circles are important for EAW, and P_- abruptly decreases as $\partial T/\partial x$ increases as shown in Fig. 8. Therefore, increasing $\partial T/\partial x$ is effective in decreasing EAW as shown in Fig. 6.

On the other hand, the attempt number is important for WE when P_- is high. The attempt numbers are about 11, 7, and 5 for $\partial T/\partial x$ = 10, 15, and 20 K/nm, respectively, when $0.1 \le P_- \le 1$ as shown in Fig. 8. Even if the attempt number for $\partial T/\partial x$ = 20 K/nm is five, it is enough to suppress WE. Therefore, the dependence of WE on $\partial T/\partial x$ is small as shown in Fig. 6.

Next, Fig. 9 shows the dependence of SNR on H_w for various linear velocities v. A large dependence of WE and a small dependence of EAW on v can be seen. The $\tau_{min} = D_{BP}/v$ (D_{BP} = 6.8 nm) values are 1.36, 0.68, and 0.34 ns for v = 5, 10, and 20 m/s, respectively, as shown in Fig. 10. The attempt numbers are about 14, 7, and 3 for v = 5, 10, and 20 m/s, respectively, when $0.1 \le P_- \le 1$ at H_w = 10 kOe. Since the attempt number for v = 20 m/s is not sufficiently large to suppress WE, reducing v is effective in decreasing WE. In other words, reducing v is effective in increasing the writing field sensitivity.

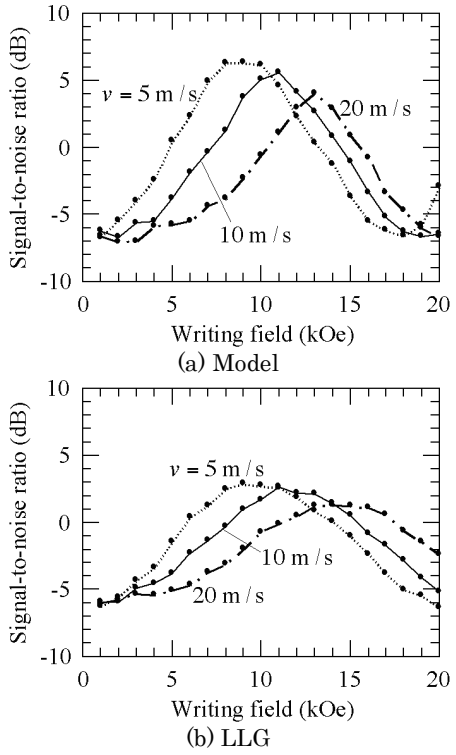

Fig. 9 Dependence of signal-to-noise ratio on writing field. (a) Model calculation and (b) micromagnetic (LLG) calculation for various v values under conditions of 1 column/bit, α = 0.1, and $\partial T/\partial x$ = 15 K/nm.

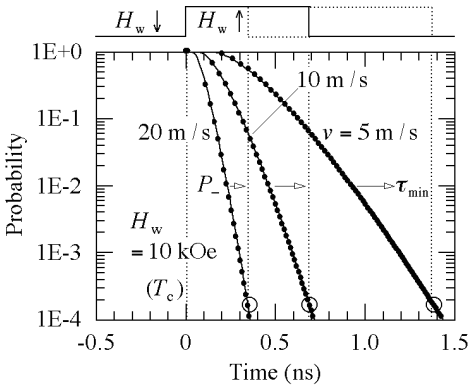

Fig. 10 Time dependence of grain magnetization reversal probability P_- for various v values under conditions of 1 column/bit, α = 0.1, and $\partial T/\partial x$ = 15 K/nm.

On the other hand, the temperatures at τ_{min} are the same regardless of the v values since the thermal gradient is constant. Then, the P_- values at τ_{min} are

the same regardless of the v values designated by open circles in Fig. 10. Therefore, the dependence of EAW on v is small.

In addition to the fact that the tendencies of the results in Figs. 6 (a) and (b) are almost the same, those in Figs. 9 (a) and (b) are also almost the same. Therefore, our model calculation can be used for HAMR design. The writing process can be described using the temperature dependences of the grain magnetization reversal probability and the attempt number in our model. A feature of our model calculation is that the interpretation of the result and the establishment of HAMR design policy are easy. Furthermore, since the calculation time of our model is short, we can calculate the bit error rate using 10^5 or 10^6 bits in a short time. Bit error rate data are useful for determining whether or not recording is possible, and our work on this topic will be published elsewhere[12].

3.2 1 column/bit and α = 0.01

We also discuss the writing property with the damping constant α = 0.01 instead of 0.1.

Figure 11 shows representative grain magnetization patterns calculated employing our model. When α = 0.1, the surface charge summation saturated at H_w = 10 kOe, as shown in Fig. 4 (b). However, when α = 0.01, the surface charge summation increased slowly with H_w and was unsaturated even at H_w = 17 kOe, as shown in Fig. 12. Therefore, WE was dominant and writing was very difficult when α = 0.01.

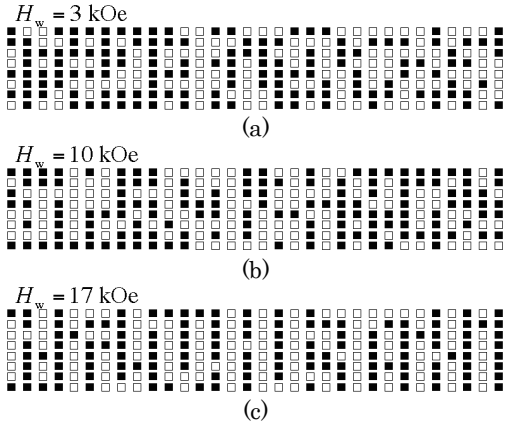

Fig. 11 Representative grain magnetization patterns for (a) H_w = 3 kOe, (b) 10 kOe, and (c) 17 kOe under conditions of 1 column/bit, α = 0.01, and typical values.

The time dependence of P_- for various H_w values is shown in Fig. 13. Although the P_- values shown in Figs. 5 and 13 are identical, the attempt number decreases to about one tenth as shown in Fig. 13, and there is almost no opportunity for writing. Therefore, WE is dominant. Since the attempt number is small when P_- is high, P_- must be increased for writing. P_- can be increased by increasing H_w in consideration of Eqs. (1) and (3). Therefore, a higher H_w is necessary when α = 0.01.

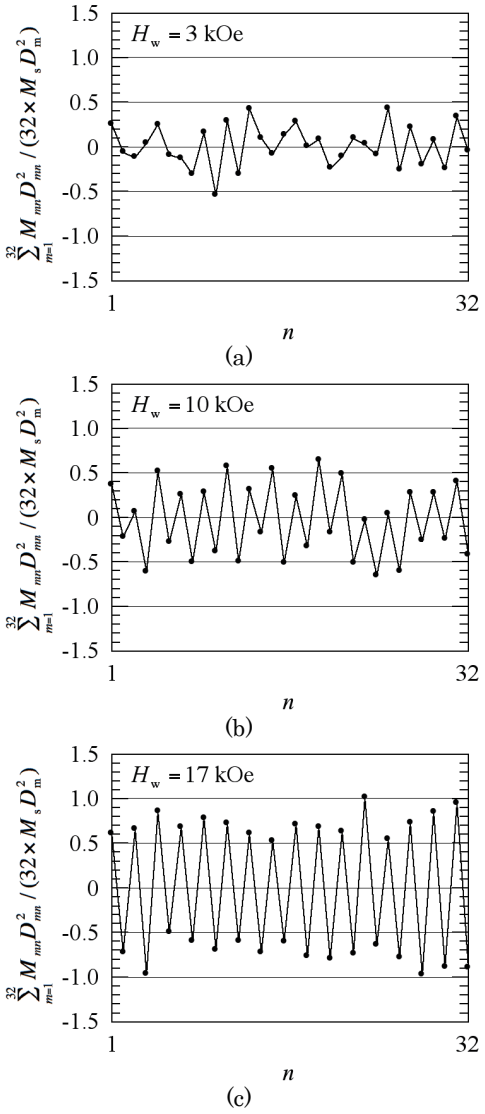

Fig. 12 Summation of surface magnetic charges $M_{mn}D_{mn}^2$ for cross-track direction m as a function of position for down-track direction n under conditions of 1 column/bit, α = 0.01, and typical values.

The dependence of SNR on H_w for various thermal gradients $\partial T/\partial x$ is shown in Fig. 14. No dependence of SNR on $\partial T/\partial x$ can be seen for either (a) Model or (b) LLG calculations since WE is dominant and changing $\partial T/\partial x$ is not effective in decreasing WE as mentioned in **3.1**.

As also mentioned in **3.1**, we expect reducing the linear velocity v to be effective in decreasing WE. Figure 15 shows the dependence of SNR on H_w for various v values regarding both (a) Model and (b) LLG calculations. As expected, when v is slow, writing becomes relatively easy since the attempt number increases from about 3 to 6 when $0 \le t \le \tau_{min}$ as v is reduced from 10 m/s to 5 m/s, as shown in Fig.

16. The decreasing SNR as H_w increases for a high H_w region in Fig. 15 is caused by EAW. EAW begins with a higher H_w than that when α = 0.1 in Fig. 9 since the attempt number for $t \geq \tau_{min}$ is also small for α = 0.01 as shown in Fig. 16. EAW in Fig. 15 (a) begins with a lower H_w than that in Fig. 15 (b). This is also attributed to the determination method of the attempt time as described in **3.1**.

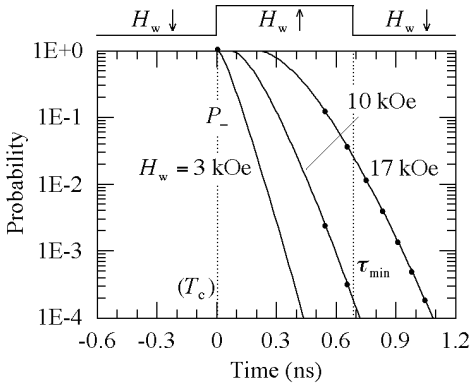

Fig. 13 Time dependence of grain magnetization reversal probability P_- for various H_w values under conditions of 1 column/bit, α = 0.01, and typical values.

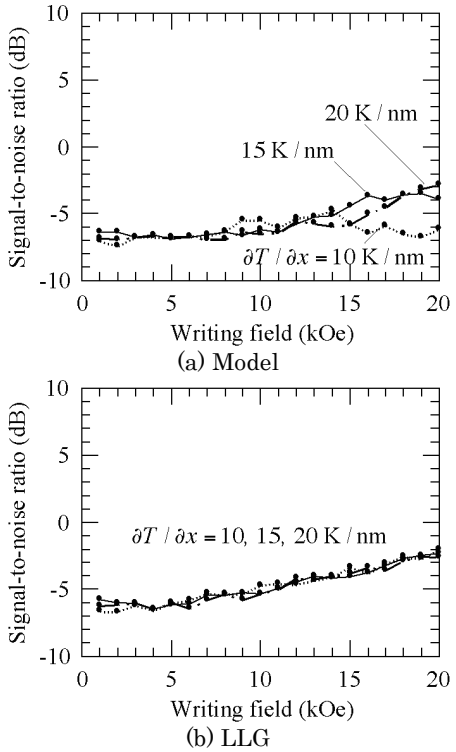

Fig. 14 Dependence of signal-to-noise ratio on writing field. (a) Model calculation and (b) micromagnetic (LLG) calculation for various $\partial T / \partial x$ values under conditions of 1 column/bit, α = 0.01, and v = 10 m/s.

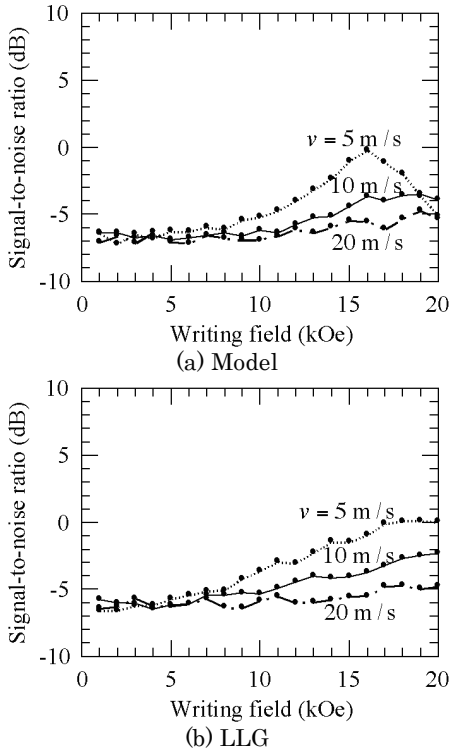

Fig. 15 Dependence of signal-to-noise ratio on writing field. (a) Model calculation and (b) micromagnetic (LLG) calculation for various v values under conditions of 1 column/bit, α = 0.01, and $\partial T / \partial x$ = 15 K/nm.

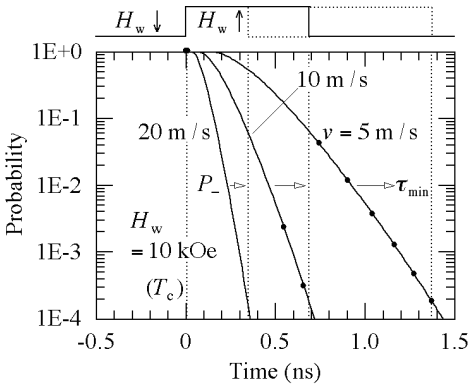

Fig. 16 Time dependence of grain magnetization reversal probability P_- for various v values under conditions of α = 0.01, and $\partial T / \partial x$ = 15 K/nm.

A serious problem in HAMR is that writing becomes difficult if the damping constant just below the Curie temperature is small. Whether or not writing is possible can be determined only by the bit error rate. Although the bit error rate data will be published elsewhere[12], the bit error rate for the medium with α = 0.01 is very high.

3.3 4 columns/bit and α = 0.1

Next, we discuss the writing property for 4 columns/bit instead of 1 column/bit.

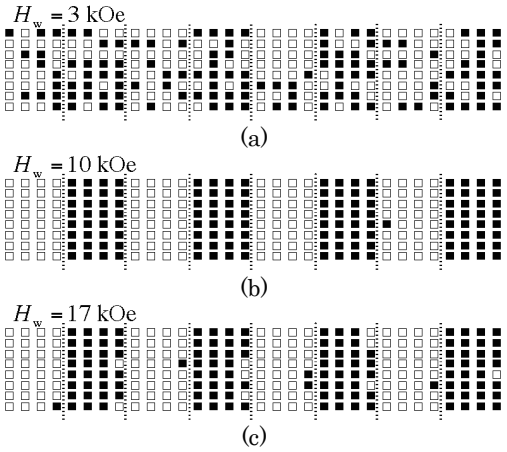

Fig. 17 Representative grain magnetization patterns for (a) H_w = 3 kOe, (b) 10 kOe, and (c) 17 kOe under conditions of 4 columns/bit, α = 0.1, and typical values. Dotted lines indicate bit boundaries.

Representative grain magnetization patterns calculated employing our model are shown in Fig. 17. The dotted lines indicate bit boundaries. In Fig. 17 (a) the writing field H_w = 3 kOe, write-error (WE) for 4 columns/bit is almost the same as that for 1 column/bit as shown in Fig. 3 (a). The H_w value of about 10 kOe is also the best condition for 4 columns/bit (see Fig. 20 (a)). However, when H_w = 17 kOe, the degradation of the grain magnetization pattern caused by erasure-after-write (EAW) for 4 columns/bit as shown in Fig. 17 (c) is remarkably small compared with that for 1 column/bit as shown in Fig. 3 (c). EAW occurs only at the 4th column in one bit as shown in Fig. 17 (c). This is confirmed by the summation of the surface magnetic charge $M_{mn}D_{mn}^2$ as shown in Figs. 4 and 18. The surface charge summation is unsaturated only at the 4th column in one bit as shown in Fig. 18 (c) according to the grain magnetization patterns for Fig. 17 (c). The same phenomenon can be seen in a previous paper[13].

This can be explained using the time dependence of the grain magnetization reversal probability P_- for H_w = 17 kOe as shown in Fig. 19. The times corresponding to the Curie temperatures T_{c1}, T_{c2}, T_{c3}, and T_{c4} are 0, 0.68, 1.37, and 2.05 ns for the 1st, 2nd, 3rd, and 4th column, respectively, and the end of the writing time τ_{min} is 2.73 ns. Therefore, the writing time for the 1st column is 2.73 ns (= 2.73 – 0 ns). Since the writing time is long, P_- for the 1st column at τ_{min} is sufficiently low and EAW does not occur. Similarly, the writing times for the 2nd and 3rd column are 2.05 (= 2.73 – 0.68) and 1.36 ns (= 2.73 – 1.37 ns), respectively. EAW does not occur since the writing times are long. However, the writing time for the 4th column is only 0.68 ns (= 2.73 – 2.05 ns), which is the same as in Fig. 5. Therefore, EAW occurs only at the 4th column in one bit since P_- at τ_{min} designated by an open circle is insufficiently low only for the 4th column.

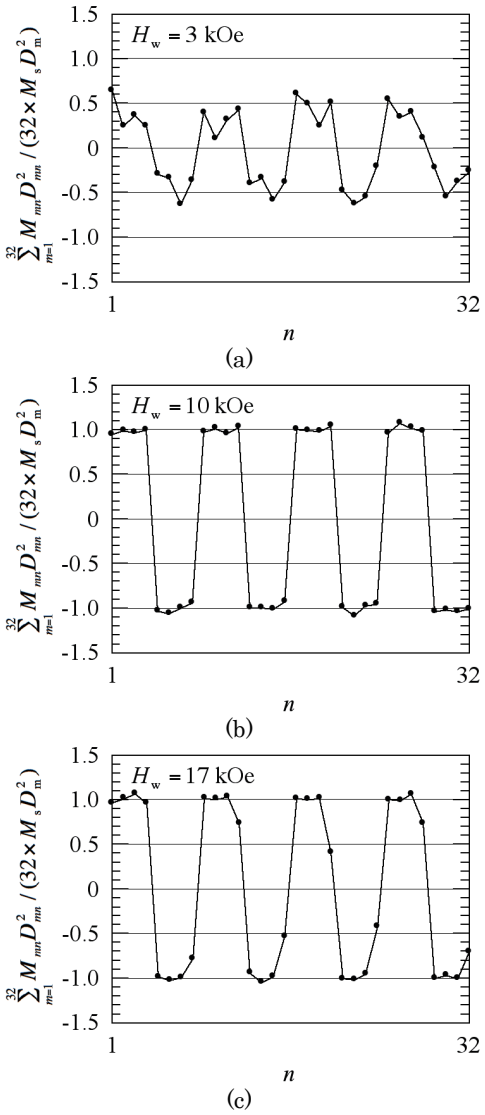

Fig. 18 Summation of surface magnetic charges $M_{mn}D_{mn}^2$ for cross-track direction m as a function of position for down-track direction n under conditions of 4 columns/bit, α = 0.1, and typical values.

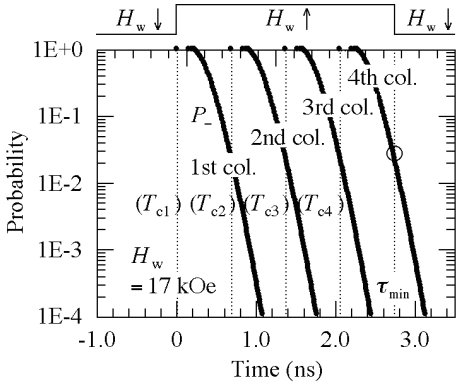

Fig. 19 Time dependence of grain magnetization reversal probability P_- for H_w = 17 kOe under conditions of 4 columns/bit, α = 0.1, and typical values.

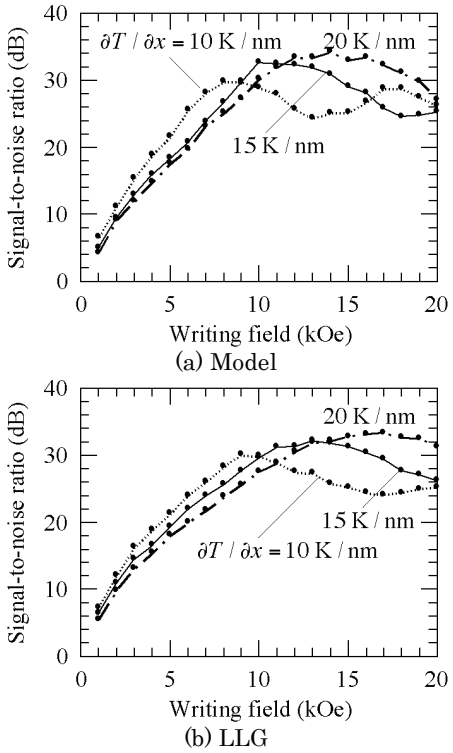

Fig. 20 Dependence of signal-to-noise ratio on writing field. (a) Model calculation and (b) micromagnetic (LLG) calculation for various $\partial T/\partial x$ values under conditions of 4 columns/bit, α = 0.1, and v = 10 m/s.

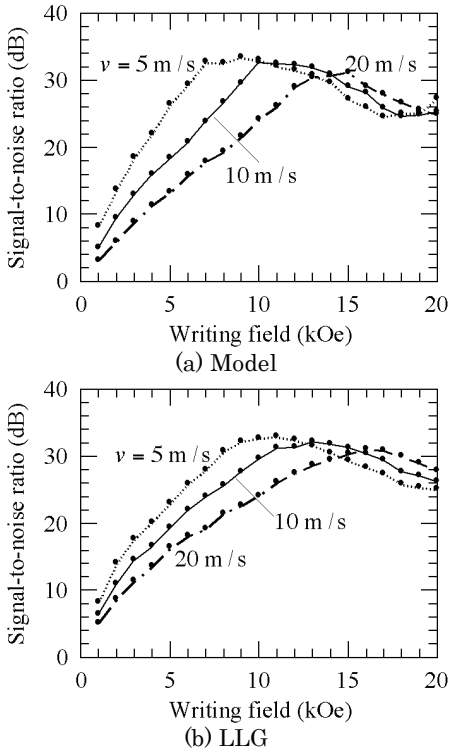

Fig. 21 Dependence of signal-to-noise ratio on writing field. (a) Model calculation and (b) micromagnetic (LLG) calculation for various v values under conditions of 4 columns/bit, α = 0.1, and $\partial T/\partial x$ = 15 K/nm.

Figure 20 shows the dependence of SNR on H_w for various thermal gradients $\partial T/\partial x$. Since increasing $\partial T/\partial x$ is effective in decreasing EAW as mentioned in **3.1**, this effect can be seen in Fig. 20. However, the SNR improvement for EAW realized by increasing $\partial T/\partial x$ is small since EAW occurs only in the 4th column. EAW and AW in Fig. 20 (a) begin with a lower H_w than that in Fig. 20 (b). This is also attributed to the determination method of the attempt time as described in **3.1**.

On the other hand, WE occurs in every column[2]. Therefore, decreasing linear velocity v is effective in improving the SNR for WE as shown in Fig. 21. In other words, reducing v is effective in increasing the writing field sensitivity.

The SNR values necessary for a certain value of bit error rate (bER), for example 10^{-3}, are approximately the same for 1 and 4 columns/bit. The SNR value for 4 columns/bit is higher than that for 1 column/bit. This implies that the writing field necessary for bER = 10^{-3} decreases and the writing field sensitivity increases as the column number increases. This issue is a statistics problem and will be discussed elsewhere[12].

3.4 4 columns/bit and α = 0.01

Finally, we discuss the writing properties for 4 columns/bit and α = 0.01.

Representative grain magnetization patterns calculated employing our model are shown in Fig. 22. Although EAW can be seen only in the 4th column in Fig. 17 (c) for α = 0.1 and H_w = 17 kOe, error occurs in every column in Fig. 22 (c) for α = 0.01 and H_w = 17 kOe. Furthermore, the surface charge summation increases as H_w increases as shown in Fig. 23. Therefore, WE is dominant even for H_w = 17 kOe.

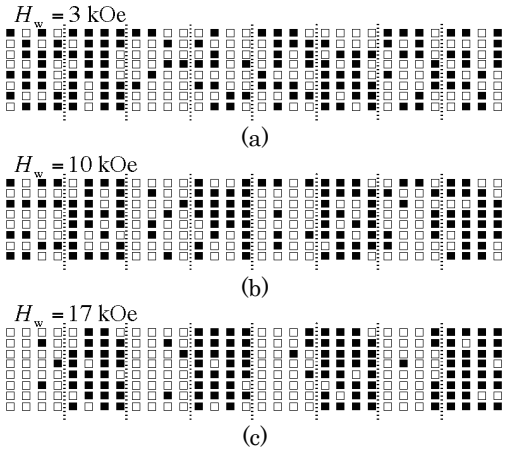

Fig. 22 Representative grain magnetization patterns for (a) H_w = 3 kOe, (b) 10 kOe, and (c) 17 kOe under conditions of 4 columns/bit, α = 0.01, and typical values. Dotted lines indicate bit boundaries.

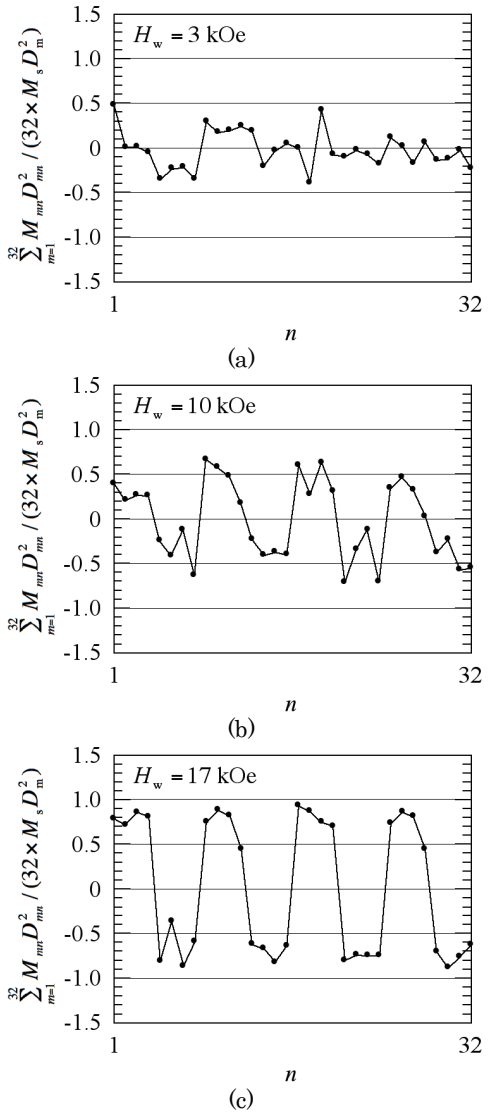

Fig. 23 Summation of surface magnetic charges $M_{mn}D_{mn}^2$ for cross-track direction m as a function of position for down-track direction n under conditions of 4 columns/bit, α = 0.01, and typical values.

The dependence of SNR on H_w for various thermal gradients $\partial T/\partial x$ is shown in Fig. 24, and for various linear velocities v in Fig. 25. Since WE is dominant, no SNR improvement in $\partial T/\partial x$ or improvement in v can be seen in Figs. 24 and 25, respectively.

The SNR value for 4 columns/bit and α = 0.01 is higher than that for 1 column/bit and α = 0.01. Therefore, writing becomes possible for 4 columns/bit even if α = 0.01. This issue is also a statistics problem and will be discussed elsewhere[12].

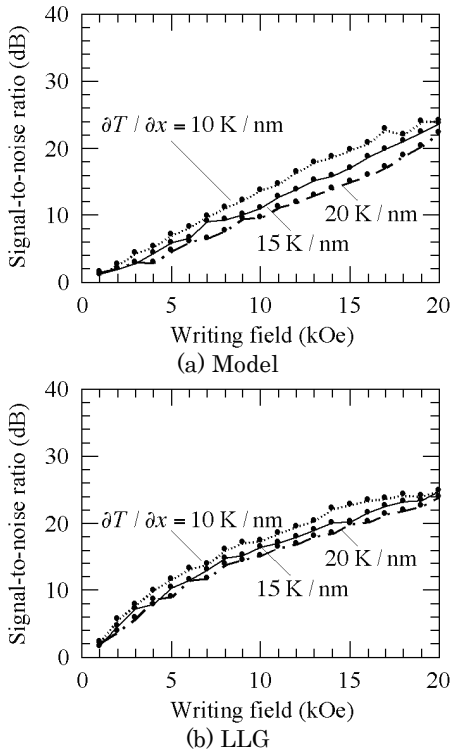

Fig. 24 Dependence of signal-to-noise ratio on writing field. (a) Model calculation and (b) micromagnetic (LLG) calculation for various $\partial T/\partial x$ values under conditions of 4 columns/bit, α = 0.01, and v = 10 m/s.

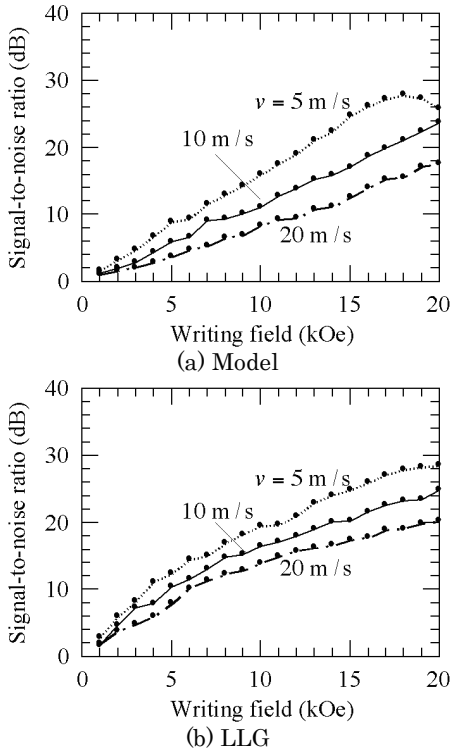

Fig. 25 Dependence of signal-to-noise ratio on writing field. (a) Model calculation and (b) micromagnetic (LLG) calculation for various v values under conditions of 4 columns/bit, α = 0.01, and $\partial T/\partial x$ = 15 K/nm.

4. Conclusions

We calculated the dependence of the signal-to-noise ratio on the writing field for heat-assisted magnetic recording (HAMR) for various calculation parameters by employing both our improved model calculation and the conventionally used micromagnetic calculation. The tendencies of the results in the model calculation and the micromagnetic calculation were almost the same. Therefore, our model calculation can be used for HAMR design. The writing process can be described using the temperature dependences of the grain magnetization reversal probability and the attempt number.

If the Gilbert damping constant is small, writing is difficult and a higher writing field is necessary since the attempt number is small.

Write-errors can be reduced by reducing the linear velocity since the attempt number increases when the grain magnetization reversal probability is high.

Erasure-after-write can be reduced by increasing the thermal gradient and/or the grain column number since the grain magnetization reversal probability becomes low at the end of the writing time.

Acknowledgement We acknowledge the support of the Advanced Storage Research Consortium (ASRC), Japan.

References

1) S. H. Charap, P. -L. Lu, and Y. He: *IEEE Trans. Magn.*, **33**, 978 (1997).
2) T. Kobayashi, F. Inukai, K. Enomoto, and Y. Fujiwara: *J. Magn. Soc. Jpn.*, **41**, 1 (2017).
3) T. Kobayashi, Y. Nakatani, F. Inukai, K. Enomoto, and Y. Fujiwara: *J. Magn. Soc. Jpn.*, **41**, 52 (2017).
4) T. Kobayashi, Y. Nakatani, K. Enomoto, and Y. Fujiwara: *J. Magn. Soc. Jpn.*, **42**, 15 (2018).
5) T. Kobayashi, Y. Isowaki, and Y. Fujiwara: *J. Magn. Soc. Jpn.*, **40**, 28 (2016).
6) T. Kobayashi, Y. Isowaki, and Y. Fujiwara: *J. Magn. Soc. Jpn.*, **39**, 8 (2015).
7) M. Mansuripur, and M. F. Ruane: *IEEE Trans. Magn.*, **MAG-22**, 33 (1986).
8) J. -U. Thiele, K. R. Coffey, M. F. Toney, J. A. Hedstrom, and A. J. Kellock: *J. Appl. Phys.*, **91**, 6595 (2002).
9) Y. Nakatani, Y. Uesaka, N. Hayashi, and H. Fukushima: *J. Magn. Magn. Mat.*, **168**, 347 (1997).
10) E. D. Boerner and H. N. Bertram: *IEEE Trans. Magn.*, **34**, 1678 (1998).
11) Y. Kanai, Y. Jinbo, T. Tsukamoto, S. J. Greaves, K. Yoshida, and H. Muraoka: *IEEE. Trans. Magn.*, **46**, 715 (2010).
12) T. Kobayashi, Y. Nakatani, and Y. Fujiwara: *J. Magn. Soc. Jpn.*, **42**, 110 (2018).
13) J. -G. Zhu and H. Li: *IEEE. Trans. Magn.*, **49**, 765 (2013).

Received Apr. 11, 2018; Accepted Aug. 31, 2018

Editorial Committee Members・Paper Committee Members

Notice for Photocopying

編 集 委 員・論 文 委 員

複写をされる方へ

Journal of the Magnetics Society of Japan

Vol. 42 No. 6 (通巻第 300 号) 2018 年 11 月 1 日発行

Vol. 42 No. 6 Published Nov. 1, 2018
by the Magnetics Society of Japan
Tokyo YWCA building Rm207, 1–8–11 Kanda surugadai, Chiyoda-ku, Tokyo 101–0062
Tel. +81–3–5281–0106 Fax. +81–3–5281–0107

Printed by JP Corporation Co., Ltd.
2–3–36, Minamikase, Saiwai-ku, Kanagawa 212–0055
Advertising agency: Kagaku Gijutsu-sha

発行：（公社）日本磁気学会 101–0062 東京都千代田区神田駿河台 1–8–11 東京YWCA会館 207 号室
製作：ジェイピーコーポレーション 212–0055 神奈川県川崎市幸区南加瀬 2–3–36 Tel.（044）571–5815
広告取扱い：科学技術社 111–0052 東京都台東区柳橋 2–10–8 武田ビル 4F Tel.（03）5809–1132